

## Dynamic Fluorescence Anisotropy Imaging Microscopy in the Frequency Domain (rFLIM)

Andrew H. A. Clayton, Quentin S. Hanley, Donna J. Arndt-Jovin, Vinod Subramaniam, and Thomas M. Jovin  
Department of Molecular Biology, Max Planck Institute for Biophysical Chemistry, D-37077 Göttingen, Germany

**ABSTRACT** We describe a novel variant of fluorescence lifetime imaging microscopy (FLIM), denoted anisotropy-FLIM or rFLIM, which enables the wide-field measurement of the anisotropy decay of fluorophores on a pixel-by-pixel basis. We adapted existing frequency-domain FLIM technology for rFLIM by introducing linear polarizers in the excitation and emission paths. The phase delay and intensity ratios (AC and DC) between the polarized components of the fluorescence signal are recorded, leading to estimations of rotational correlation times and limiting anisotropies. Theory is developed that allows all the parameters of the hindered rotator model to be extracted from measurements carried out at a single modulation frequency. Two-dimensional image detection with a sensitive CCD camera provides wide-field imaging of dynamic depolarization with parallel interrogation of different compartments of a complex biological structure such as a cell. The concepts and technique of rFLIM are illustrated with a fluorophore-solvent (fluorescein-glycerol) system as a model for isotropic rotational dynamics and with bacteria expressing enhanced green fluorescent protein (EGFP) exhibiting depolarization due to homotransfer of electronic excitation energy (emFRET). The frequency-domain formalism was extended to cover the phenomenon of emFRET and yielded data consistent with a concentration depolarization mechanism resulting from the high intracellular concentration of EGFP. These investigations establish rFLIM as a powerful tool for cellular imaging based on rotational dynamics and molecular proximity.

### INTRODUCTION

The fluorescence anisotropy ( $r$ ) of intrinsic or extrinsic fluorophores provides valuable information about the state and environment of the corresponding biomolecular carrier on or within a cell. The steady-state anisotropy,  $\bar{r}$ , of a distinct molecular species undergoing isotropic rotational diffusion is related to the excited state lifetime  $\tau$  and the rotational correlation time  $\phi$  according to the Jablonski equation (Jablonski, 1960),

$$\frac{r_o}{\bar{r}} = 1 + \frac{\tau}{\phi} = 1 + \sigma, \quad (1)$$

where  $r_o$  is a limiting value (in the absence of rotation) given by the relative orientation of the absorption and emission transition moments, and  $\sigma$  is the ratio  $\tau/\phi$ . From Eq. 1, it follows that the anisotropy is a parameter with the capability of revealing changes in orientational distribution and in the excited state lifetime with great sensitivity. Such

a circumstance arises readily in cell biology, e.g., from alterations in local microviscosity or other restrictions to diffusional motion, biochemical environment, complex formation, and molecular proximity manifested by hetero- or homo-transfer of electronic energy. Furthermore, the fluorescence anisotropy and lifetime are both intrinsic parameters, unlike the intensity signals used to determine them, and are thereby relatively insensitive to experimental factors such as light path and geometry. This fortunate circumstance permits more reliable comparisons between data obtained from different experiments and from different laboratories.

The measurement of fluorescence anisotropy in a microscope offers the possibility for characterizing very small domains on the surface or in the interior of the cell. For example, the cytoplasmic viscosity of living cells was determined by anisotropy imaging of fluid-phase fluorophores (Dix and Verkman, 1990). In addition, highly oriented samples, such as labeled protein constituents of the plasma membrane, can be readily visualized by anisotropy microscopy, as documented in the pioneering study by Axelrod (1979) of the orientational distribution of dyes bound to erythrocyte ghost membranes.

Measurements of dynamic depolarization or anisotropy decay provide additional and complementary information, such as rotational correlation times sensitive to the rotational volume and shape of the fluorophore. Anisotropy decay can reveal the multiplicity of rotational correlation times reflecting heterogeneity in the molecular population and in the size, shape, and internal motions of the fluorophore–biomolecule conjugate. Real molecules often exhibit molecular asymmetry, anisotropic rotational modes, and multiple lifetimes, and, in the cellular milieu, molecular

*Submitted April 20, 2001, and accepted for publication April 19, 2002.*

Address reprint requests to Thomas M. Jovin, Department of Molecular Biology, Max Planck Institute for Biophysical Chemistry, Am Fassberg 11, D-37077 Göttingen, Germany. Tel.: +49-551-201-1382; Fax: +49-551-201-1467; E-mail: tjovin@gwdg.de.

A.H.A. Clayton's present address is Ludwig Institute for Cancer Research, P.O. Box 2008, Royal Melbourne Hospital, Parkville, Victoria 3050, Australia.

Q.S. Hanley's present address is Dept. of Chemical and Biological Sciences, Univ. of the West Indies, Cave Hill Campus, St. Michael, Barbados.

V. Subramaniam's present address is Advanced Science and Technology Laboratory, Bldg. 80, AstraZeneca R&D Charnwood, Bakewell Rd, Loughborough, Leicestershire LE11 5RH, U.K.

© by the Biophysical Society

0006-3495/02/09/1631/19 \$2.00

heterogeneity is the rule rather than the exception. An adequate mathematical formulation of such systems is necessarily complex, as is already evident from Eq. 1 due to the dependence of  $\bar{r}$  on three other parameters. The need to image the dynamic depolarization of fluorophores in cellular environments directly prompted the present investigation.

Determinations of rotational correlation times are performed either in the time or frequency domain. For example, using an excitation pulse as a forcing function, Eq. 1 is transformed into a decay process in which the fluorescence lifetime  $\tau$  is no longer linked to the correlation time  $\phi$

$$r(t) = (r_0 - r_\infty)e^{-t/\phi} + r_\infty, \quad i(t) = e^{-t/\tau}, \quad (2)$$

where  $i(t)$  is the instantaneous emission intensity, normalized to a unit integrated value. In Eq. 2, the parameter  $r_\infty$  reflects the extent to which the rotational reorientation is hindered. An example is the case of a transmembrane protein undergoing molecular rotation in a lipid bilayer (Lipari and Szabo, 1980; Kinosita et al., 1982; Thevenin et al., 1994; Martin-Fernandez et al., 1998). For this case,  $\bar{r}$  is obtained by integrating the intensity-weighted  $r(t)$  (Eq. 3); the same approach applies to heterogeneous systems and more complex (multiexponential, nonexponential) time courses for the decay of the excited state or rotational diffusion,

$$\bar{r} = \int_0^\infty r(t) \cdot i(t) dt \rightarrow \frac{r_0 - r_\infty}{\bar{r} - r_\infty} = 1 + \sigma. \quad (3)$$

By itself, the fluorescence lifetime is of great value for the generation of contrast in fluorescence microscopy. Fluorescence lifetime imaging microscopy (FLIM) provides pixel-by-pixel discrimination among fluorophores differing in excited state kinetics due to distinct photophysical characteristics or microenvironments. FLIM has been implemented with time-domain (Wang et al., 1991; Ghigginio et al., 1992; Scully et al., 1997; Cole et al., 2000) and frequency-domain (Marriot et al., 1991; Lakowicz et al., 1992; Piston et al., 1992; Gadella et al., 1993; Squire et al., 2000; Verveer et al., 2000; Hanley et al., 2001) techniques.

We have undertaken the extension of the FLIM technology to include the generation of images based on the dynamic depolarization of fluorescence, and denote the approach featured in this report as anisotropy FLIM (rFLIM). rFLIM complements standard steady-state polarization microscopy (Axelrod, 1979) and corresponding static and dynamic polarization measurements performed in solution or suspension. It adds the imaging capability to previous systems that were limited to single-point anisotropy decay measurements in the microscope (Verkman et al., 1990; Martin-Fernandez et al., 1998; Tramier et al., 2000).

The implementation of rFLIM with two-dimensional (2D) image detection using a sensitive charge-coupled de-

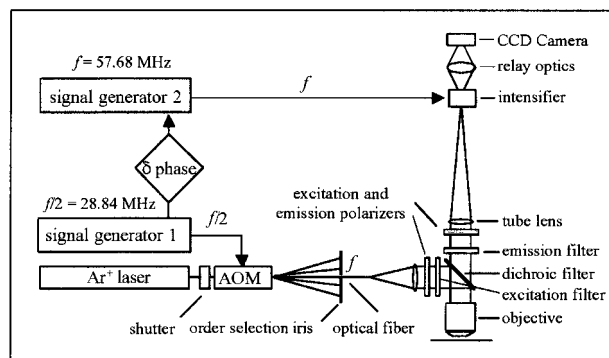


FIGURE 1 Schematic of rFLIM apparatus. The microchannel plate intensifier was modulated at the photocathode. The signal generators driving the image intensifier and the acousto-optical modulator (AOM) were phase locked to a 10-MHz frequency standard. The relative phase ( $\delta$  phase) between the two was adjusted under computer control, cycling through a series of  $n$  phase steps of  $360^\circ/n$ . An image was recorded at each phase step. The zero-order light exiting the AOM was isolated from the higher orders by an iris and relayed to the microscope illumination system through a multimode optical fiber. The optical modulation frequency was double the AOM driving frequency.

vice (CCD) camera provides wide-field imaging of dynamic depolarization, e.g., with the intent of simultaneously interrogating different compartments of a cell. To this end, we modified a frequency-domain FLIM apparatus (Gadella et al., 1993; Schneider and Clegg, 1997; Hanley et al., 2001) by the introduction of linear polarizers in the excitation and emission paths (Fig. 1). In this report, we first describe our experimental implementation of rFLIM and then the theory of frequency-domain rotational dynamics extended to rFLIM. The latter is illustrated with dynamic depolarization measurements of fluorescein in glycerol/water mixtures and of enhanced green fluorescent protein (EGFP) in bacteria. Finally, we discuss other applications, limitations, and future perspectives of rFLIM.

## EXPERIMENTAL

### rFLIM apparatus

A schematic of the rFLIM instrument is shown in Fig. 1. The frequency domain fluorescence lifetime and rotational dynamics imaging instrument was built as an add-on to a standard research grade fluorescence microscope (E-600, Nikon, Düsseldorf, Germany). The FLIM system used as the basis for the measurement of rotational dynamics was similar to previously described instruments (Gadella et al., 1993; Schneider and Clegg, 1997; Hanley et al., 2001). A modulated image intensifier (model C5825, Hamamatsu Photonics, Herrsching, Germany) was installed on the camera port of the microscope. The modulation frequency and phase were set with a computer-controlled signal generator (model 2030; Marconi Instruments, St. Albans, UK). The intensified image was relayed to a 14-bit cooled CCD camera (model KX-2 containing a Kodak KAF-1600 CCD with  $9\text{-}\mu\text{m}$  square pixels in a  $1536 \times 1024$  format; Apogee Instruments, Tucson, AZ) using a tandem pair of  $f/1.8$  (AF Nikkor, Nikon) camera lenses. The 488-nm line of an  $\text{Ar}^+$  ion laser (Innova 90-5; Coherent, Santa Clara, CA) was used to illuminate the microscope field. The laser light was modulated by an acousto-optic modulator (AOM) (model SWM-10044; IntraAction

Corp., Belwood, IL). A second signal generator (model 2023; Marconi) was frequency and phase locked to the intensifier signal generator. Its output signal was amplified with a 37-dB broadband linear power amplifier (model 403LA; Electronic Navigation Industries, Rochester, NY) and used to drive the AOM at a frequency in most experiments of 28.84 MHz, leading to optical modulation at  $f = 57.68$  MHz. The zero-order light from the AOM was selected and relayed through a multimode optical fiber (model CU-3578 UV-vis; Multimode Fiber Optics, East Hanover, NJ) to the microscope illumination port. The optical fiber was vibrated mechanically at audio frequencies to scramble modes and thus reduce speckle. The dichroic filter was a 505 DRLP02 and the emission longpass filter ( $>515$  nm) a 515EFLP (Omega Optical, Brattleboro, VT).

Anisotropy measurements were implemented by the addition of a sheet polarizer (Y-FA, Nikon) to the excitation light source and an analyzer (PW44, Schott, Mainz, Germany; or a Polaroid film polarizer) on the emission path of the microscope oriented either parallel or perpendicular to the excitation beam polarizer. Three data sets were taken; a conventional lifetime image with both excitation and emission polarizers removed; a  $0^\circ/0^\circ$  (excitation/emission) polarization image; and a  $0^\circ/90^\circ$  polarization image. A lifetime and anisotropy standard,  $1 \mu\text{M}$  aqueous rhodamine 6G (Hanley et al., 2001), was also measured to provide a pixel-by-pixel calibration of relative modulation depth, phase shift, and polarization dependent transmissions ( $G$ -factor, Eq. 4 below).

## Polarization confocal laser scanning microscopy

Confocal polarization-dependent images of the EGFP-expressing bacteria were acquired with a modified LSM 310 confocal laser scanning microscope (model LSM310; Zeiss, Göttingen, Germany), equipped with an external  $\text{Ar}^+$  ion laser (80 mW, 488 nm) as a photobleaching source. Fluorescence images of the parallel and perpendicular emission of the bacterial embedded in agarose were recorded with a  $63\times$  (1.2 NA) C-Apochromat water immersion objective, using excitation at 488 nm and emission at  $>515$  nm. The unpolarized emission of a  $0.2 \mu\text{M}$  fluorescein solution served to calculate the instrument  $G$ -factor (1.23) under the same conditions.

The total fluorescence and anisotropy images were generated with Scil-Image (TNO TPD, Delft, The Netherlands) software after background subtraction and pixel registration of the two polarized emission images by cross-correlation analysis. The final anisotropy image was smoothed by a  $3 \times 3$  uniform filter function. Background pixels were excluded by threshold masking. The mean  $r$  for each anisotropy image was calculated from the mean intensity-weighted pixel values. Measurements were performed at ambient temperature ( $23^\circ\text{C}$ ).

## Data acquisition and processing in rFLIM

In our implementation of rFLIM, the excitation light and the detector (intensifier) gain were modulated by the same radial frequency  $\omega$ . A series of images was acquired while adjusting the relative phase between the AOM and the intensifier (Fig. 1) over one period ( $2\pi$  radians,  $360^\circ$ ). The images were taken in sets of  $n$  ( $n = 4, 8, \text{ or } 16$ ) such that each successive image was measured with an incremental phase shift of  $360^\circ/n$ . Each series of images was accompanied by a corresponding blank image acquired with all shutters open except for the laser source. Acquisition proceeded with a reversal of the sequence of phase shifts for achieving a first-order photobleaching compensation; the second data series was processed as a second period of the sampled sinusoidal waveform. Acquisition was the same for sample, standard, and all polarization states. Two sets of measurements were made with the emission polarizer oriented either parallel or perpendicular. Each data set was processed (Hanley et al., 2001) to yield frequency-dependent amplitudes, and a phase shift between the excitation and the emitted light. The two resulting polarized emission components are modulated at the same frequency but phase shifted relative to each other;  $I_{\perp,AC}$

leads  $I_{\perp,AC}$  by  $\Delta\Phi$ . In addition, the AC amplitude of the perpendicular component is reduced relative to that of the parallel component. These signals are characterized by the ratio  $Y_{AC} = I_{\parallel,AC}/I_{\perp,AC}$ , and the corresponding ratio of DC ( $\omega = 0$ ) magnitudes by  $Y_{DC} = I_{\parallel,DC}/I_{\perp,DC}$ .

Processing of the data involved five steps. 1) The lifetime images were computed from data obtained for the sample and lifetime reference in the absence of polarization optics. 2) The  $\Delta\Phi$ ,  $Y_{AC}$ , and  $Y_{DC}$  images were calculated for the sample data sets. 3) The equivalent standardization images were computed for use as diagnostics and for determining  $G$ -factor corrections. 4) The latter were applied to the  $Y_{AC}$ , and  $Y_{DC}$  images according to the procedures given below. 5) Images of the anisotropy parameters ( $\phi$ ,  $r_\parallel$ ,  $r_\perp$ ) were generated according to the formalism developed in the Results section (Eqs. 14, 18–20, 24–27).

The pixel-by-pixel corrections to the amplitude images ( $Y_{AC}$ ,  $Y_{DC}$ ) were based on measurements of a reference solution with known anisotropy.  $G$ -factors ( $G_i$ ) accounting for differences in system response for the two polarized emission components were computed at each ( $i$ th) image pixel using a reference solution of known anisotropy (usually  $\sim 0$ ), according to

$$G_i = \left( \frac{1 + 2\bar{r}_{\text{ref}}}{1 - \bar{r}_{\text{ref}}} \right) \frac{1}{Y_{DC,i}^{\text{ref}}}, \quad (4)$$

where  $\bar{r}_{\text{ref}}$  is the steady-state anisotropy of the reference solution measured in a spectrofluorometer and  $Y_{DC,i}^{\text{ref}}$  is the DC intensity ratio ( $I_{\parallel,i}/I_{\perp,i}$ ) of the polarized emission measured in the microscope (see also Dix and Verkman, 1990). The reference measurements were made either directly before or after the sample measurement with identical optical configuration (objective, dichroic filter, etc.). The values of  $G_i$  were  $1.15 \pm 0.08$  [Plan  $2\times$  (NA 0.06) air objective] and differed by less than 0.02 among the different objectives tested [Plan  $2\times$ , PlanFluor  $20\times$  (NA 0.75) air, PlanFluor  $40\times$  (NA 0.75) air, Plan Apo  $60\times$  (NA 1.2) water]. The corrected AC and DC ratios of the sample were obtained from

$$Y_{(AC,DC),i}^{\text{corr}} = G_i \cdot Y_{(AC,DC),i}^{\text{meas}}. \quad (5)$$

We observed a zero phase shift (within experimental error) for excitation with unpolarized light. Consequently, no corrections for instrumental effects on the phase shift were required. The programs Scil-Image (TNO TPD) and *Mathematica* 4.0 (Wolfram Research, Champaign, IL), including the Digital Imaging Processing add-on, were used for further image processing (segmentation and masking), generation of frequency histograms, and statistical analyses. Regions of interest (corresponding to individual cuvettes in a dual cuvette image or a particular cellular compartment in the cells) were isolated using an image intensity threshold mask.

## Reference measurements in a spectrofluorometer

The fluorescence anisotropies of fluorescein solutions in glycerol–buffer mixtures and of rhodamine 6G in water were determined at  $23^\circ\text{C}$  with a commercial spectrofluorometer (enhanced model C-60, Photon Technology International, Monmouth Junction, NJ). The excitation wavelength was 488 nm, the emission wavelength 540 nm, and the slit spectral bandwidth 5 nm. For the rhodamine 6G solution,  $\bar{r}_{\text{ref}}$  was 0.012.

The fluorescence anisotropy and relative peak intensities of EGFP solutions were determined at  $20^\circ\text{C}$  with a Cary Eclipse spectrofluorometer (Varian Australia Pty, Melbourne) equipped with motorized excitation and emission polarizers. The excitation wavelength varied between 450 and 480 nm, and the emission spectra were measured up to 600 nm with a 5-nm bandwidth. A Suprasil cuvette with a 0.25-mm square cross section ( $<1 \mu\text{L}$  fill volume) was used to minimize inner filter and reabsorption effects. The intensity values were corrected for absorption  $A$  along the lightpath by the factor  $A \ln[10]/(1 - 10^{-A})$ . Anisotropy values determined in the two spectrofluorimeters agreed within 5%.

## Materials and EGFP-expressing bacteria

Glycerol–buffer solutions over a range of glycerol concentrations from 10 to 80% (w/w) were prepared gravimetrically using spectroscopic grade glycerol (Aldrich, Milwaukee, WI) and 10 mM Tris-HCl, pH 8.0. Solutions for rFLIM rotational correlation time measurements contained 10, 61, and 70% glycerol by weight. The viscosities ( $\eta$ , 23°C) of these solutions (1.2, 10.6, 21.3 cP, respectively) were estimated from published tables (Weast, 1979). Solutions for viscosity-dependent fluorescence measurements were prepared by addition of a small volume (<50  $\mu$ L) of  $\sim$ 2 mM fluorescein in ethanol to a cuvette containing the glycerol/buffer mixture. The solutions were not deoxygenated. EGFP solutions were prepared volumetrically in 0.1 M Tris-HCl, 0.1 M NaCl, pH 8.5 buffer by dilution from a stock solution of known concentration, based on the extinction coefficient at 490 nm of 55 mM<sup>-1</sup>cm<sup>-1</sup> (Patterson et al., 1997); we used  $\epsilon_{480\text{nm}} = 50 \text{ mM}^{-1}$ .

*Escherichia coli* bacteria expressing EGFP were cultured at 37°C as described previously (Jakobs et al., 2000). Before rFLIM measurements, the bacteria were suspended in 1% agarose to minimize movement and mounted between a microscope slide and a coverslip. Some of the EGFP leaked into the extracellular medium. A sample from the same bacterial culture was centrifuged and the supernatant was found to contain free EGFP, the spectral properties of which were identical to those obtained by deliberate lysis of the bacteria via repeated freeze–thaw cycles. The mean concentration of intracellular EGFP was estimated by filtration of the bacterial suspension over a Millipore HA 0.45  $\mu$  nitrocellulose filter. The weight of the packed cells corresponding to a given volume of culture medium was determined and the EGFP fluorescence of the suspension and filtrate compared to a known (2.8  $\mu$ M EGFP) reference solution.

## RESULTS

### Theory

We first examine the theory of anisotropy and dynamic depolarization as applied to standard cuvette-based measurements of randomly orientated fluorophores using a homodyne measurement scheme. In conventional instruments, the sample is excited with linearly polarized light. The emission is detected perpendicular to the excitation propagation direction and viewed through an analyzing polarizer oriented either parallel ( $I_{\parallel}$ ) or perpendicular ( $I_{\perp}$ ) to the excitation beam polarizer. These two signals differ in general because the polarized incident beam generates an anisotropic distribution of excited state fluorophores, i.e., by photoselection (Albrecht, 1961). Rotational diffusion of the fluorophores during the excited

The theory underlying the determination of rotational correlation times, differential polarized phase fluorometry, a method introduced by Weber and coworkers, is found in several excellent papers and reviews (Weber, 1977, 1978; Mantulin and Weber, 1977; Lakowicz et al., 1979; Lakowicz 1983; Jameson and Hazlett, 1986). The three measured parameters ( $\Delta\Phi$ ,  $Y_{AC}$ ,  $Y_{DC}$ ) reflect the excited state lifetime and/or the intrinsic rotational diffusion properties of the fluorophore (and its conjugate) (Eq. 2), and an experimental variable (the modulation frequency  $\omega$ ) that can be manipulated at will.

For the hindered rotator represented by Eq. 2 and using our nomenclature, one obtains

$$\Delta\Phi = \tan^{-1} \left[ \frac{3 \cdot \omega\tau \cdot \sigma \cdot (r_o - r_{\infty})}{(1 - r_o)(1 + 2r_o)[1 + (\omega\tau)^2] + [2 + r_o - r_{\infty}(4r_o - 1)]\sigma + (1 - r_{\infty})(1 + 2r_{\infty})\sigma^2} \right], \quad (7)$$

$$Y_{AC} = \sqrt{\frac{(1 + 2r_o)^2(\omega\tau)^2 + [(1 + 2r_o) + (1 + 2r_{\infty})\sigma]^2}{(1 - r_o)^2(\omega\tau)^2 + [(1 - r_o) + (1 - r_{\infty})\sigma]^2}}, \quad (8)$$

$$Y_{DC} = \frac{1 + 2r_o + (1 + 2r_{\infty})\sigma}{1 - r_o + (1 - r_{\infty})\sigma}; \quad \bar{r} = \frac{Y_{DC} - 1}{Y_{DC} + 2}. \quad (9)$$

Note that we have used the dimensionless variables  $\omega\tau$  and  $\sigma$ , incorporating  $\tau$  and  $\phi$ . That is, the rotational correlation time is expressed relative to the lifetime and the latter serves to scale the radial frequency. Our parameters differ from those used in the early publications ( $R = 1/(6\phi)$ , Weber, 1977, 1978; Lakowicz et al., 1979). The relationships of Eqs. 7–9 are depicted in Fig. 2 as a function of  $\omega\tau$  and  $\sigma$ . The phase difference  $\Delta\Phi$  approaches 0 at both extremes of frequency ( $\omega = 0, \infty$ ) and passes through a maximum, whereas  $Y_{AC}$  increases monotonically with  $\omega$ , albeit to a degree dependent on  $\sigma$ ;  $Y_{DC}$  is not a function of frequency. The maximal value of  $\Delta\Phi$ , for any given parameter set ( $r_o, r_{\infty}, \sigma$ ), is given by (Weber, 1978)

$$\Delta\Phi_{\text{max}, \omega\tau} = \tan^{-1} \left[ \frac{3(r_o - r_{\infty})\sigma}{2\sqrt{(1 - r_o)(1 + 2r_o)[1 - r_o + (1 - r_{\infty})\sigma][1 + 2r_o + (1 + 2r_{\infty})\sigma]}} \right], \quad (10)$$

state lifetime reduces the disparity between  $I_{\parallel}$  and  $I_{\perp}$ , resulting in dynamic depolarization of the emitted light according to Eq. 2. The fluorescence anisotropy  $r(t)$  at any time point is defined as (Jablonski, 1960)

$$r(t) = \frac{I_{\parallel}(t) - I_{\perp}(t)}{I_{\parallel}(t) + 2I_{\perp}(t)}. \quad (6)$$

with

$$\omega\tau_{\Delta\Phi\text{max}} = \sqrt{\left(1 + \frac{(1 - r_{\infty})}{(1 - r_o)}\sigma\right) \left(1 + \frac{(1 + 2r_{\infty})}{(1 + 2r_o)}\sigma\right)} \approx 1 + \sigma, \quad (11)$$

and, for any given parameter set ( $r_o, r_{\infty}, \omega\tau$ ), by

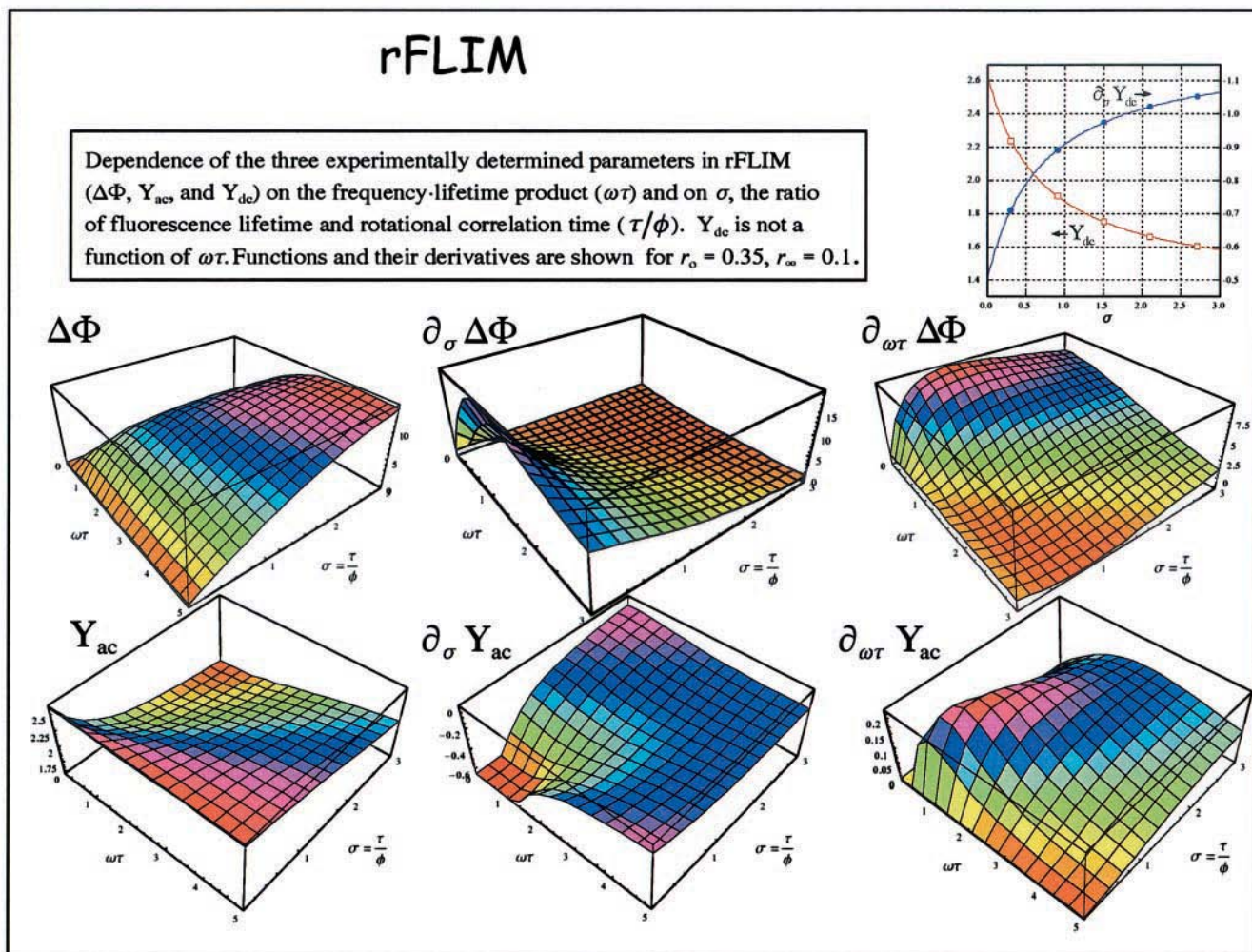


FIGURE 2 Dependence of rFLIM measured parameters ( $\Delta\Phi$ ,  $Y_{AC}$ ,  $Y_{DC}$ ) and their partial derivatives on  $\omega\tau$  and  $\sigma$ . See text for discussion.

$$\Delta\Phi_{\max,\sigma} = \tan^{-1} \left[ \frac{3(r_o - r_\infty)\omega\tau}{2 + r_o - r_\infty(4r_o - 1) + 2\sqrt{[(1 - r_o)(1 + 2r_o)(1 - r_\infty)(1 + 2r_\infty)(1 + (\omega\tau)^2)]}} \right], \quad (12)$$

with

$$\sigma_{\Delta\Phi_{\max}} = \sqrt{\frac{(1 - r_o)(1 + 2r_o)[1 + (\omega\tau)^2]}{(1 - r_\infty)(1 + 2r_\infty)}} \approx \sqrt{1 + (\omega\tau)^2}. \quad (13)$$

The approximations of Eqs. 11 and 13 hold well ( $\pm 10\%$ ) over a large range of  $r_o$  and  $r_\infty$  values. Thus, a frequency sweep of  $\Delta\Phi$  can provide an estimate of  $\sigma$  (Eq. 11) and, thereby, of  $\phi$ .

The dependence of  $\Delta\Phi$ ,  $Y_{AC}$ , and  $Y_{DC}$  on  $\sigma$  is also featured in the three-dimensional (3D) representations of Fig. 2.  $\Delta\Phi$  is a bell-shaped function of  $\sigma$  (a limited region of parameter

space is shown in Fig. A1).  $Y_{DC}$  and  $Y_{AC}$  decrease monotonically with  $\sigma$ . (These properties apply for  $r_o > r_\infty > 0$ .) Important features of these parametric functions are revealed by the partial derivatives of  $\Delta\Phi$ ,  $Y_{AC}$ , and  $Y_{DC}$  with respect to  $\omega\tau$  and  $\sigma$ , which are also functions of the same two parameters (Fig. 2). The greatest measurement sensitivity is achieved for the largest magnitudes of the derivatives, i.e., at low values of  $\sigma$  and  $\omega$ . However, the optimal conditions for determining  $\phi$  are not necessarily the same as those for  $\tau$ . It follows that a judicious choice of experimental conditions is required for the most sensitive determination of  $\phi$ .

The expressions corresponding to an isotropic rotator are given by setting  $r_\infty$  to 0 in Eqs. 7–9 (and in Eqs. 14–19

below). In the practical application of Eqs. 7–9,  $\tau$  is obtained from independent measurements, and  $\phi$  is derived from various strategies for achieving solutions for  $\sigma$  (and thus  $\phi$  via the definition  $\sigma = \tau/\phi$ ). The approaches depend on the model and differ according to the degree of prior knowledge about the other depolarization parameters ( $r_o$  and  $r_\infty$ ) and the selection of signals (Eqs. 7–9) to be used alone or in combination.

The general solutions of Eqs. 7–9 for  $\sigma$  (and thus for  $\phi$ ) consist of the following expressions (Eqs. 14–19). The program *Mathematica* was used to perform extensive symbolic manipulations and simulations of these functions. The solution derived from difference phase measurements is given by

$$\phi_{\Delta\Phi} = \frac{a}{1 + \text{sign} \sqrt{b}} \cdot \tau \quad (14)$$

with

$$a = \frac{2(1 - r_\infty)(1 + 2r_\infty)\tan \Delta\Phi}{3(r_o - r_\infty)\omega\tau - [2 + r_o(1 - 4r_\infty) + r_\infty]\tan \Delta\Phi}, \quad (15)$$

$$b = 1 - \frac{(1 - r_o)(1 + 2r_o)}{(1 - r_\infty)(1 + 2r_\infty)} [1 + (\omega\tau)^2] a^2 \\ = 1 - \sigma_{\Delta\Phi\text{max}}^2 a^2, \quad (16)$$

$$\text{sign} = - \quad \text{if } \sigma < \sigma_{\Delta\Phi\text{max}} \text{ (Eq. 13);} \\ + \quad \text{for } \sigma > \sigma_{\Delta\Phi\text{max}}. \quad (17)$$

In experimental practice, it is best to select a frequency for which  $\sigma_{\Delta\Phi\text{max}}$  is not close to  $\sigma$  because  $b$ , the argument of the square root function of Eq. 14, vanishes for this condition. Experimental error in the determination of  $\Delta\Phi$  can lead to fluctuations of  $b$  about 0, including negative values, and thus render evaluations of Eq. 14 problematical due to the presence of complex numbers. However, a good approximation holds for  $|b| \approx 0$ :  $\phi_{\Delta\Phi} \approx \tau/\sigma_{\Delta\Phi\text{max}}$ . For  $\sigma_{\Delta\Phi\text{max}} \neq \sigma$ ,  $b$  can still be driven negative in the event that experimental noise generates a recorded  $\Delta\Phi$  exceeding the value of  $\Delta\Phi_{\text{exact}}$  (given by Eq. 7) by a factor  $> [(\Delta\Phi_{\text{max},\sigma}/\Delta\Phi_{\text{exact}}) - 1]$ . In such cases,  $\phi_{\Delta\Phi}$  is mathematically and physically indeterminate, inasmuch as all solutions are imaginary.

The solutions derived from the AC and DC components of the relative polarized signals are given by

$$\phi_{Y_{\text{DC}}} = \left[ \frac{Y_{\text{DC}}(1 - r_\infty) - (1 + 2r_\infty)}{(1 + 2r_o) - Y_{\text{DC}}(1 - r_o)} \right] \cdot \tau. \quad (19)$$

In the simplest application of Eqs. 14–19,  $r_\infty$  is set to zero and  $r_o$  is fixed at an independently-determined value. Next, the rotational correlation times derived from the three experimental signals are compared. In general, agreement among the three values indicates that the system behaves as an isotropic rotator. Disagreement implies more complex modes of anisotropy decay. Values determined in this manner are apparent rotational correlation times and serve as a very simple measure of rotational correlation time heterogeneity. In the event that either  $r_o$  or  $r_\infty$  are known, different solutions can be derived by combination of any two of Eqs. 7–9. For example, for the hindered rotator model, knowledge of  $r_o$  (a relatively invariant photophysical quantity) provides a solution for variable  $\Delta\Phi$  (i.e.,  $\phi$ ) and  $r_\infty$  using the  $\Delta\Phi$  and  $Y_{\text{DC}}$  (or as an equivalent,  $\bar{r}$ , in Eq. 9) signals.

$$\phi_{\Delta\Phi,\bar{r}} = \frac{a}{1 + \text{sign} \sqrt{b}} \cdot \tau, \quad (20)$$

with

$$a = \left[ \frac{3(r_o - \bar{r})\omega\tau}{2(1 - \bar{r})(1 + 2\bar{r})\tan \Delta\Phi} - 1 \right]^{-1}, \quad (21)$$

$b =$

$$\frac{9(\bar{r} - r_o)^2 - 4(1 - \bar{r})(1 + 2\bar{r})(1 - r_o)(1 + 2r_o)\tan \Delta\Phi^2}{[2(1 - \bar{r})(1 + 2\bar{r})\tan \Delta\Phi - 3(r_o - \bar{r})\omega\tau]^2} (\omega\tau)^2, \quad (22)$$

$$\text{sign} = + \quad \text{if } \frac{(1 + \sqrt{b})\tau}{(r_o/\bar{r} - 1)} > a > \left( \frac{1 + \sqrt{b}}{1 - \sqrt{b}} \right) a \\ - \quad \text{otherwise}, \quad (23)$$

$$r_\infty = \frac{(\bar{r} - r_o)}{\sigma_{\Delta\Phi,\bar{r}}} + \bar{r} = (\bar{r} - r_o) \left( \frac{\phi_{\Delta\Phi,\bar{r}}}{\tau} \right) + \bar{r}. \quad (24)$$

A similar approach was advocated by Lakowicz et al. (1979) to determine hindered rotations of a membrane probe in lipid bilayers.

$$\phi_{Y_{\text{AC}}} = \frac{Y_{\text{AC}}^2(1 - r_\infty)^2 - (1 + 2r_\infty)^2}{(1 + 2r_o)(1 + 2r_\infty) - Y_{\text{AC}}^2(1 - r_o)(1 - r_\infty)} \cdot \tau \quad (18) \\ + \sqrt{Y_{\text{AC}}^2 \left\{ 9(r_o - r_\infty)^2 + \left[ 2 + r_\infty(2 + 5r_\infty) + r_o[2 - 4r_\infty(4 + r_\infty)] \right. \right. \\ \left. \left. + r_o^2[5 - 4r_\infty(1 - 2r_\infty)] - Y_{\text{AC}}^2(1 - r_o)^2(1 - r_\infty)^2 \right] (\omega\tau)^2 \right\} \\ - (1 + 2r_o)^2(1 + 2r_\infty)^2(\omega\tau)^2}$$

### Composite expressions for rotational diffusion parameters

Equations related to those presented above have appeared in the literature in different forms. They share the disadvantage of requiring some prior knowledge of  $r_o$  and/or  $r_\infty$ , information that may not be readily available in microscope-based studies. However, combining all three parameters ( $\Delta\Phi$ ,  $Y_{AC}$ ,  $Y_{DC}$ ; Eqs. 7–9) and  $\tau$  leads to independent “composite” expressions (Eqs. 25–27) for the three rotational diffusion parameters.

$$\phi^{\text{comp}} = \left[ \frac{Y_{AC}[(Y_{AC}^2 - 2Y_{DC})(Y_{DC} + 2)\sqrt{1 + \tan^2 \Delta\Phi^2} + Y_{AC}(Y_{DC} - 4)]\tan \Delta\Phi \cdot \omega\tau}{(Y_{AC}^2 - 4)(Y_{AC}^2 - Y_{DC}^2) + (Y_{AC}^2 - 2Y_{DC})^2 \tan^2 \Delta\Phi^2} - 1 \right]^{-1} \cdot \tau, \quad (25)$$

$$r_o^{\text{comp}} = \frac{(Y_{AC}^2 + 2)(Y_{AC}^2 - Y_{DC}^2) + (Y_{AC}^2 - 2Y_{DC})(Y_{AC}^2 + Y_{DC})\tan \Delta\Phi^2 - 3Y_{AC}(Y_{AC}^2 - Y_{DC}^2)\sqrt{1 + \tan^2 \Delta\Phi^2}}{(Y_{AC}^2 - 4)(Y_{AC}^2 - Y_{DC}^2) + (Y_{AC}^2 - 2Y_{DC})^2 \tan^2 \Delta\Phi^2}, \quad (26)$$

$$r_\infty^{\text{comp}} = \frac{\left( (Y_{AC}^2 + 2)(Y_{AC}^2 - Y_{DC}^2) - 3Y_{AC}[Y_{AC}^2 - Y_{DC}^2 - (Y_{AC}^2 + Y_{DC}^2)\tan \Delta\Phi \cdot \omega\tau]\sqrt{1 + \tan^2 \Delta\Phi^2} \right.}{\left. - Y_{AC}^2[2(Y_{DC}^2 + 2) + (Y_{DC} - 1)(Y_{DC} + 2)\tan \Delta\Phi \cdot \omega\tau]\tan \Delta\Phi \cdot \omega\tau + (Y_{AC}^2 - 2Y_{DC})(Y_{AC}^2 + Y_{DC})\tan \Delta\Phi^2 \right)}{(Y_{AC}^2 - 4)(Y_{AC}^2 - Y_{DC}^2) - Y_{AC}^2[2(Y_{DC}^2 - 4) + (Y_{DC} + 2)^2 \tan \Delta\Phi \cdot \omega\tau]\tan \Delta\Phi \cdot \omega\tau + (Y_{AC}^2 - 2Y_{DC})^2 \tan^2 \Delta\Phi^2}. \quad (27)$$

Note that  $r_o^{\text{comp}}$  does not depend explicitly on either the fluorescence lifetime or the modulation frequency; an implicit dependence is via  $\Delta\Phi$ ,  $Y_{AC}$ , and  $Y_{DC}$  (Eqs. 7–9). This parameter may well be invariant in a given system under investigation, suggesting that a global analysis over an entire image would provide a constant mean value for use in Eq. 20. This procedure also minimizes quantitative discrepancies by ensuring that the same optical configuration applies to all parameters. Others have noted that distortions to the anisotropy decay induced by high NA objectives are mainly manifested in changes in the  $r_o$  and not  $\phi$  (Tramier et al., 2000). Thus, independent self-consistent measures of  $r_o$  and  $\phi$  are desirable.

In this study, the above formalism was applied to images acquired in the fluorescence microscope and with pixel-by-pixel resolution. The apparent correlation times computed according to the above formalism were used to characterize the system and detect heterogeneity with respect to the correlation time and degree of hindered rotation. In the presence of heterogeneity, including that of the intensity decay function (multiple lifetimes), one must resort to more complex models and multi-frequency measurements, as has been described for FLIM (Squire et al., 2000). If some, but not all, parameters are constant over the sample, a global analysis can also be implemented, as in the case of single-frequency FLIM determinations (Verveer et al., 2000). It is evident that the influence of propagated measurement error

will vary among the various approaches represented in Eqs. 14–27.

The above equations are valid provided a unique or appropriate mean fluorescence lifetime can be defined. Fluorophores with monoexponential decays yield equivalent phase and modulation lifetimes. This condition does not hold for more complex decay functions, requiring a more elaborate formalism for the selection of an appropriate lifetime average (e.g., a combination of phase and modulation values) for use in the above equations. However, the latter approach fails if molecular association(s) leads to a

coupling of multicomponent intensity and anisotropy decay processes (Szmecinski et al., 1987; Jameson and Sawyer, 1995).

### Concentration depolarization due to homotransfer Fluorescence Resonance Energy Transfer (emFRET)

In addition to depolarization by rotational diffusion, the emission anisotropy decreases in the event that excitation energy is transferred between nearby molecules during the excited state lifetime. Concentration depolarization due to FRET between identical molecules is a well-documented phenomenon (Bojarski and Sienicki, 1989) that occurs in concentrated solutions of fluorophores exhibiting a finite Stokes shift. In cell biological studies, homotransfer FRET (which we designate here as emFRET) has been applied to the analysis of protein oligomerization on the plasma membrane (Varma and Mayor, 1998; Blackman et al., 1998; Bene et al., 2000) and within the cell (Gautier et al., 2001). In the latter case, emFRET of EGFP fused to viral thymidine kinase was measured by time-correlated single photon anisotropy decay.

We sought to implement emFRET by the wide-field rFLIM imaging technique. To do so, we extended the phase-modulation frequency domain formalism presented above to include provision for the excited state process (Lakowicz

and Balter, 1982) of energy migration. For the specific experimental case treated here, that of emFRET involving EGFP in free solution, the extent of rotational depolarization during the excited state lifetime is limited ( $\sigma < 1$ ) and a good approximation for the apparent composite anisotropy decay (diffusion + energy migration) is given by the product of the terms representing the two processes (see Fig. 4 of Engstrom et al., 1992). In this case, the impulse response functions (Eq. 1) corresponding to the parallel and perpendicular emission components and for the case of an unhindered spherical rotator are given by

$$I_{\parallel,\perp}(t) = \frac{e^{-t/\tau}}{3\tau} [1 + \gamma_{\parallel,\perp} r_o e^{-t/\phi} e^{-\alpha c(t/\tau)^{1/2}}], \quad (28)$$

where  $\gamma_{\parallel} = 2$  and  $\gamma_{\perp} = -1$ ,  $c$  is the fluorophore concentration (in mM units), and  $\alpha$ , the coefficient of the  $c(t/\tau)^{1/2}$  term accounting for energy migration, is given (in  $\text{mM}^{-1}$  units) by

$$\alpha = 2 \cdot 10^{-27} \pi \sqrt{\pi/3} N_{\text{av}} \langle |\kappa| \rangle R_o^3 \approx (R_o^3/375), \quad (29)$$

where  $R_o$  is the characteristic Förster transfer distance (50% transfer efficiency for a single donor–acceptor FRET pair; units, nm),  $N_{\text{av}}$  is Avogadro's constant, and  $\langle |\kappa| \rangle$  ( $= 0.69$ ) is the orientation-averaged square root of the Förster orientation factor  $\kappa^2$ . This formulation assumes a random initial static distribution of molecular transition moments and a completely depolarized emission from any but the initially excited molecule. The ensemble excited state lifetime remains unaltered in emFRET.

The steady-state anisotropy is obtained by integration of Eq. 28, yielding

$$\bar{r} = \frac{r_o}{1 + \sigma} [1 - \beta e^{\beta^2} \pi^{1/2} \text{erfc}(\beta)], \quad (30)$$

where

$$\beta = \frac{\alpha c}{2\sqrt{1 + \sigma}}. \quad (31)$$

The convolution of Eq. 28 with a sinusoidal modulating function leads to analytical equations for the difference phase and modulation corresponding to Eqs. 7–9 but including the effect of energy migration, represented by the parameter  $\alpha$ . A detailed analysis will be given elsewhere. However, the effect of emFRET on  $\Delta\Phi$  and  $Y_{\text{AC}}$  can be summarized as follows:  $\Delta\Phi$  increases and then decreases with  $c$ , particularly for high modulation frequencies and low values of  $\sigma$ ; and  $Y_{\text{AC}}$  decreases at all frequencies.

### Determination of fluorescence anisotropy in the microscope

Conventional descriptions of fluorescence anisotropy apply most readily to standard solution measurements of fluoro-

**TABLE 1** Effect of objective lens numerical aperture on rFLIM parameters ( $\Delta\Phi$ ,  $Y_{\text{AC}}$ ,  $\bar{r}$ ) for fluorescein in 80% (w/w) glycerol/buffer

Objective (Nikon)	NA	$\Delta\Phi$ (°)	$Y_{\text{AC}}$ *	$\bar{r}$
Fluorometer				0.24
Plan 2×, air†	0.06	11 ± 1	2.27 ± 0.02	0.24 ± 0.03
Plan 2×, air‡	0.06	11 ± 1	2.27 ± 0.02	0.24 ± 0.03
Plan Fluor 20×, air†	0.50	11 ± 1	nd	nd
Plan Fluor 40×, air†	0.75	11 ± 1	nd	nd
Plan Apo 60×, water‡	1.20	11 ± 2	2.13 ± 0.02	0.22 ± 0.03

\*Optical modulation frequency, 58 MHz.

†1-cm quartz cuvette.

‡Sample chamber with cover slip.

A  $G$ -factor correction (1.15) was determined with the Plan 2×, air objective and applied to all microscope measurements. Fluorometer: excitation, 488 nm, emission, 540 nm. Microscope: excitation, 488 nm, emission 520–560 nm.

nd, not determined.

phores with random orientations in the ground state and detection of the emission with the conventional 90° narrow-aperture configuration, i.e., orthogonal to the propagation direction of the excitation beam. In the microscope, one has to deal with the particular excitation/detection configurations including epi-illumination, high numerical apertures, nonrandom orientations in the ground state (Axelrod, 1979; Florine-Casteel, 1990; Fushimi et al., 1990), polarization distortions produced by biases or birefringence in the optical components (i.e., objectives, apertures, reflectors, filters, prisms: Axelrod, 1979; Florine-Casteel, 1990; Dix and Verkman, 1990; Bahlmann and Hell, 2000; Tramier et al., 2000) and detectors, and photobleaching under conditions of high irradiance.

The perturbation by high numerical aperture (NA) illumination/collection optics of polarization states characteristic of plane waves is manifested by mixing of polarization components along the three optical axes (Jovin, 1979; Axelrod, 1979, 1989; Florine-Casteel, 1990; Dix and Verkman, 1990; Sheppard and Torok, 1997; Bahlmann and Hell, 2000; Tramier et al., 2000). According to Axelrod (1989), the contribution of the observed polarization components of the emission can be formulated as linear sums of products of axial distributions dependent on sample properties and weighting factors that are functions of the NA. We have examined these effects empirically by assessing the influence of NA on the steady-state anisotropies and phase-shifts of known samples.

## EXPERIMENTAL RESULTS

### Microscope validation

Steady-state anisotropies of fluorescein solutions of varying viscosity (achieved by addition of glycerol) were measured in the imaging microscope and compared to the corresponding values obtained in a spectrofluorometer. In general, the

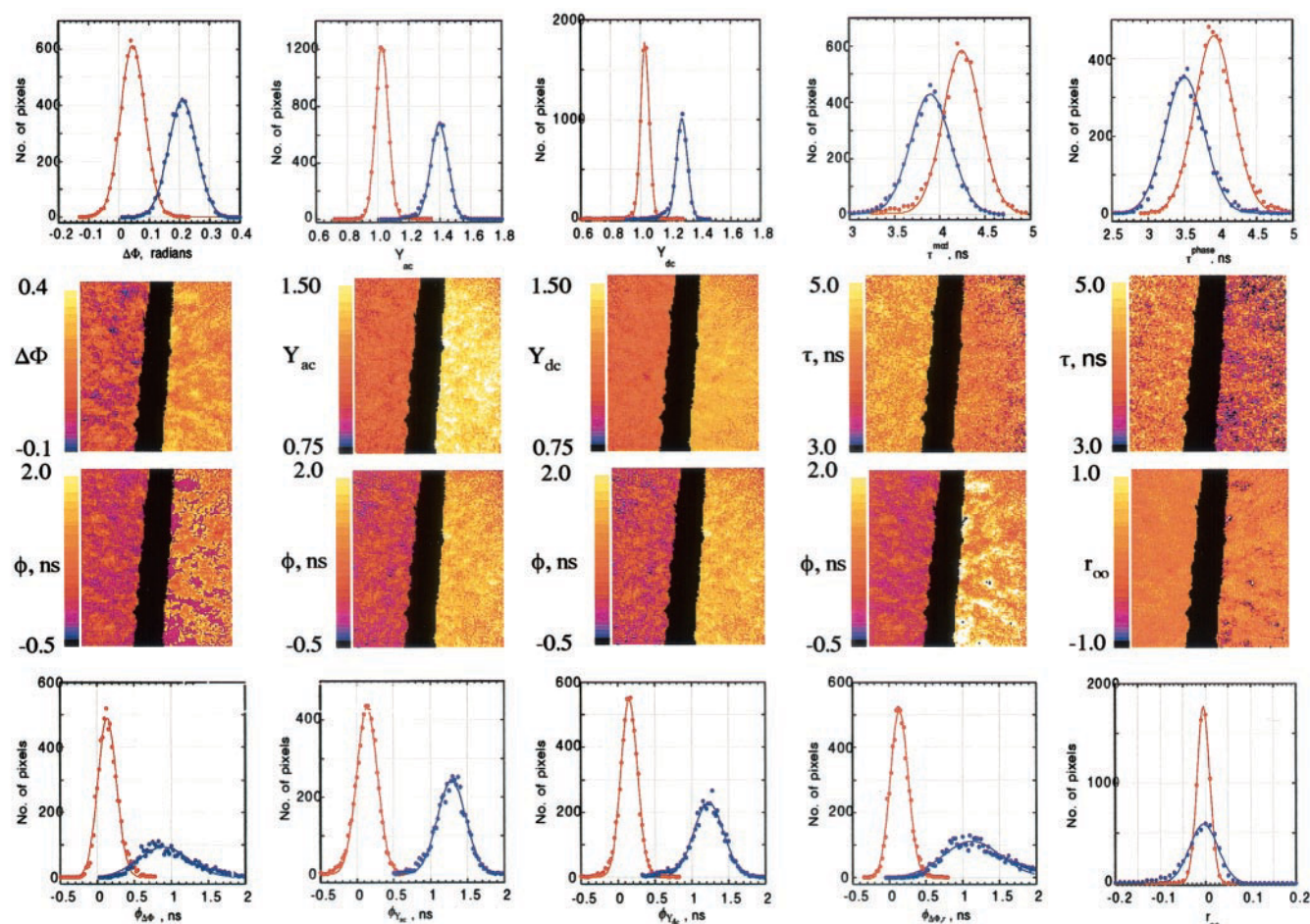


FIGURE 3 Spatially-resolved FLIM and rFLIM of fluorescein solutions containing 10% and 61% glycerol. Solutions in adjacent cuvettes: 10% glycerol, *left* in images and *red* in histograms; 61% glycerol, *right* in images and *blue* in histograms. *Top* and *bottom* rows, histograms corresponding to the images in the two center rows. *Symbols*, all of the binned data points; *solid lines*, Gaussian fits. Both original measured signals ( $\Delta\Phi$ ,  $Y_{AC}$ ,  $Y_{DC}$ ) and derived anisotropy parameters are shown. The objective was a Plan 2 $\times$  air (NA 0.06). See text for nomenclature and discussion.

two sets of measurement were in good agreement and could be accounted for by a single  $G$ -factor (Eq. 4). Tests for a systematic depolarization bias due to wide-aperture excitation–detection via the objective lens were also carried out. Using solutions of fluorescein in 80% glycerol, a small depolarizing effect, manifested as slight decreases in  $Y_{AC}$  and  $\bar{r}$ , was observed as the magnification and NA of the objective lens increased (Table 1). Similar results have been reported by others (Dix and Verkman, 1990; Verkman et al., 1990; Tramier et al., 2000). According to the theoretical results of Axelrod (Fig. 2 in Axelrod, 1989), the steady-state anisotropy corresponding to an isotropic rotator with  $r_o = 0.4$  and  $\sigma = 0.6$  should decrease from 0.25 to  $\sim 0.21$  as the  $NA/\eta$  value varies from 0.06 to 0.88. The variation documented in Table 1 was somewhat smaller, probably due to a contribution from out-of-focus light from the relatively thick solutions. Recent rFLIM data from cultured cells expressing GFP-tagged receptors and calibrated microspheres have revealed more pronounced NA effects (Subramaniam et al., 2002).

It is interesting that the corresponding values of  $\Delta\Phi$  in Table 1 were independent of the aperture, in accordance with the observations of Verkman et al. (1990). As expected, removal of the excitation polarizer yielded a  $\Delta\Phi = 0$  within experimental error, implying the absence of an instrumental phase lag between the parallel and perpendicular components of emission. Thus, no correction for instrumental phase shift was required.

### Single-frequency rFLIM measurements of fluorescein–glycerol solutions

As a model system for demonstrating the ability of rFLIM to image regions differing in  $\bar{r}$  and  $\phi$ , we imaged two adjacent cuvettes containing fluorescein solutions of different viscosity (10% glycerol/90% buffer,  $\eta = 1.2$  cP; 61% glycerol/39% buffer  $\eta = 10.6$  cP) and FLIM and rFLIM measurements. Figure 3 illustrates the acquired polarization data ( $\Delta\Phi$ ,  $Y_{AC}$ , and  $Y_{DC}$ ), the fluorescence lifetime values

**TABLE 2** rFLIM parameters for fluorescein in glycerol/buffer\*

Parameter	10% glycerol					61% glycerol				
	Mean <sup>†</sup>	Mean	SD	CV	SE	Mean <sup>†</sup>	Mean	SD	CV	SE
No. pixels		6329					4839			
$\tau_{\text{phase}}$ (ns)	4.12 <sup>‡</sup>	3.97	0.34	0.09	4	3.75 <sup>‡</sup>	3.57	0.44	0.12	6
$\tau_{\text{mod}}$ (ns)		4.27	0.29	0.07	4		3.92	0.26	0.07	4
$\Delta\Phi$ (rad)		0.052	0.042	0.81	0.5		0.217	0.046	0.21	0.7
$Y_{\text{AC}}$		1.03 <sub>2</sub>	0.105	0.10	1		1.40 <sub>3</sub>	0.06	0.04	0.9
$Y_{\text{DC}}$		1.02 <sub>9</sub>	0.099	0.09	1		1.28 <sub>0</sub>	0.05	0.04	0.7
$\phi_{\Delta\Phi}$ (ns)	0.15	0.15 <sub>9</sub>	0.14	0.88	2	1.21	0.89 <sub>5</sub>	0.35	0.39	5
$\phi_{Y_{\text{AC}}}$ (ns)	0.14	0.15 <sub>4</sub>	0.13	0.84	2	1.28	1.28 <sub>4</sub>	0.22	0.17	3
$\phi_{Y_{\text{DC}}}$ (ns)	0.15	0.15 <sub>3</sub>	0.13	0.85	2	1.21	1.21 <sub>7</sub>	0.25	0.21	4
$\phi_{\Delta\Phi, \bar{r}}$ (ns)	0.14	0.15 <sub>3</sub>	0.13	0.85	2	1.25	1.33	0.63	0.47	9
$r_{\infty}$	0.00	0.00	0.01			0.00	-0.01	0.04		0.6
$\phi^{\text{comp}}$ (ns)	0.14	na			na	1.56	2.29	1.76 <sup>§</sup>	0.77	30
$r_0^{\text{comp}}$	0.38	0.00	0.28		4	0.32	0.31	0.18 <sup>§</sup>	0.58	3
$r_{\infty}^{\text{comp}}$	0.00	0.00	0.06		0.8	0.00	-0.01	0.12 <sup>§</sup>		2

\*Means and standard deviations of frequency versus parameter histograms obtained from analysis of each cuvette (as segmented regions of interest in the dual-cuvette image).

<sup>†</sup>Anisotropy decay parameters derived from the means of the acquired parameters only.

<sup>‡</sup> $\tau_{\text{av}}$ , CV, coefficient of variation = SD/mean. SE ( $\times 10^3$ ), standard error = SD/ $\sqrt{\text{no. pixels}}$ .

<sup>§</sup>The  $G$ -factor image generated in the experiments depicted in Figs. 5 and 6 displayed high frequency (pixel-to-pixel variations) with an amplitude of 5–10%. These were reduced substantially by applying low-frequency filtering, nonlinear regression (Global Fit add-on to *Mathematica*) to analytical equations representing the row and column variations, and post-filtering. For example, in the case of the 61% glycerol solution, the standard deviations of the histograms of derived composite parameters (Eqs. 25–27, entries in this Table) diminished by 1–2 orders of magnitude.

na, Not applicable (negative values).

( $\tau_{\text{phase}}$  and  $\tau_{\text{mod}}$ ), and the corresponding derived quantities: the rotational correlation times [ $(\phi_{\Delta\Phi}, \phi_{Y_{\text{AC}}}, \phi_{Y_{\text{DC}}}$ ; Eqs. 14–19, with  $r_0 = 0.35, r_{\infty} = 0$ ) and  $(\phi_{\Delta\Phi, \bar{r}}, r_{\infty}$ ; Eqs. 20–24, with  $r_0 = 0.35$ )] determined at a single optical modulation frequency of 58 MHz. The mean values and standard deviations of the lifetime and anisotropy parameter distributions are collected in Table 2. Standard errors have been included as an indication of the errors in the means. The large number of pixels in the distribution led to reasonably precise estimates of the mean, and to standard errors that were typically two orders of magnitude smaller than the standard deviations. Consideration of the standard deviations and standard errors also allows an estimate of the number of pixels required to discriminate between given differences in rotational parameters. The minimal detectable difference between the means of two distributed parameters  $x$  and  $y$  is given by  $|\bar{x} - \bar{y}| = st\sqrt{(n_x + n_y)/(n_x n_y)}$ , where  $t$  is the Student's test,  $s$  is the pooled standard deviation and  $n_x, n_y$  are the population sizes. Anisotropy decay parameters computed from the means of the entire distributions ( $\Delta\Phi, Y_{\text{AC}}$ , and  $Y_{\text{DC}}$ ) for each condition are also given in Table 2.

Several points emerge from the images and histograms displayed in Fig. 3. First, spatial resolution was achieved with both acquired data and derived parameters, allowing a clear distinction among the different solutions in the two cuvettes. In general, the histograms and images showed two distinct populations based on the lifetime and anisotropy decay values. The emission of fluorescein in the 10% glycerol solution was characterized by a mean  $\tau_{\text{phase}}$  and  $\tau_{\text{mod}}$  of 4.0 and 4.3 ns, respectively, at the optical modulation fre-

quency of 58 MHz. This difference suggests a degree of heterogeneity in the fluorescence decay. Modeling the data in terms of two lifetime populations yielded an average value ( $\tau_{\text{av}}$ ) of 4.1 ns, close to the mean of the phase and modulation lifetimes. The lifetimes ( $\tau_{\text{phase}} = 3.6$  ns,  $\tau_{\text{mod}} = 3.9$  ns,  $\tau_{\text{av}} = 3.7$  ns) of the 61% glycerol solution were shorter by  $\sim 10\%$  than the values for the 10% glycerol solution.

The rotational correlation times differed significantly between the two test solutions, for all methods of calculation (Table 2). The 10% glycerol solution was characterized by a  $\phi$  of  $\sim 0.14$  ns, and the 61% glycerol solution by a  $\phi$  of  $\sim 0.9$ –1.3 ns. Despite the similar standard deviations of the images, the ratio of the mean rotational correlation times was  $\sim 8$ , compared to the lifetime value ratio of 0.9, thus attesting to the utility of rFLIM in this example. The contrast achieved in the rotational correlation time images was expected based on the difference in viscosity of the two glycerol mixtures. The lower degree of contrast in the fluorescence lifetime images is consistent with the known relative insensitivity of the fluorescein lifetime to solvent composition (Magde et al., 1999).

There were also differences between the relative amplitudes, means, and widths of the  $\phi$  histograms derived from the various individual parameters (particularly  $\Delta\Phi$  compared to  $Y_{\text{AC}}$  and  $Y_{\text{DC}}$ ). For example, we note the anomalously low value of  $\phi_{\Delta\Phi}$  of the 61% glycerol data (Table 2). In part, this result reflected the different levels of noise in the measured quantities, the exclusion of pixels yielding imaginary  $\phi_{\Delta\Phi}$  values (in the case of the 61% glycerol

solution), and the different weighting and error propagation properties associated with  $\phi_{\Delta\Phi}$  versus  $\phi_{Y_{AC}}$  and  $\phi_{Y_{DC}}$ . These effects are well rationalized by the distribution simulations and their discussion presented earlier (see Appendix). We note that the anomalous parameter derived from the phase data is not expected to occur under all experimental situations and can be suppressed by combining the phase with the modulation data or using pre-averaging of the raw parameters over regions of interest.

The various  $\phi$  values computed using the population means of the acquired parameters were much closer [Table 2: 10% glycerol (0.15, 0.14, 0.15 ns); 61% glycerol (1.21, 1.28, 1.21 ns)]. The good agreement among the three apparent rotational correlation times derived from each sub-image confirms that fluorescein behaved as an isotropic rotator in both solutions. The ratio of the means for the two solutions (8.4) was close to the ratio of the bulk viscosities (8.8), and extrapolating the data to 1 cP (water) yielded a rotational correlation time of 0.12 ns, in good agreement with literature values (0.1 ns; Periasamy and Verkman, 1992).

Analysis in terms of the hindered rotator model yielded  $r_{\infty} = 0 \pm 0.01$ , as expected for an isotropic rotator, and a rotational correlation time value in good agreement with the one derived from the analysis above (Eq. 24, Fig. 3, Table 2). The use of the combined  $r\text{-}\Delta\Phi$  analysis partially compensated for the anomalous rotational correlation time values derived from the phase measurement alone.

The calculations presented above used an  $r_o$  value of fluorescein of 0.35. Insertion of the means of the acquired parameters into the composite hindered-rotator model (Eq. 25), yielded  $r_o^{\text{comp}}$  values (10% glycerol, 0.38; 61% glycerol, 0.32; average, 0.35) that compare well with the literature value used above and rotational correlation times (Table 2) that agreed to within 0.3 ns with the other determinations. Thus, in practical applications, an image-averaged  $r_o$  (which in the ideal case is a photophysical invariant and thus expected to be constant for a given species) is recommended in cases where this parameter has not been independently determined. Calculations using the acquired parameter distributions gave variable results with the composite-hindered rotator model. The 10% glycerol calculations did not yield correct values for either  $\phi$  or  $r_o$ . However, the parameters obtained for the 61% solution were close to the correct values. These results were reproduced with numerical simulations. For an isotropic rotator with a  $\phi$  of 0.15 ns, simulated data with a (CV) better than 0.1% were required to recover the correct anisotropy parameter values. For a slower rotator with a  $\phi$  of 1.5 ns experimentally realizable CVs in the simulated data generated the correct anisotropy values. In general, the results of the composite-hindered rotator model reflected the combined noise contributions of all three experimental quantities ( $\Delta\Phi$ ,  $Y_{AC}$ ,  $Y_{DC}$ ) with  $r_o^{\text{comp}}$  being the most sensitive to noise and  $r_{\infty}^{\text{comp}}$  the least.

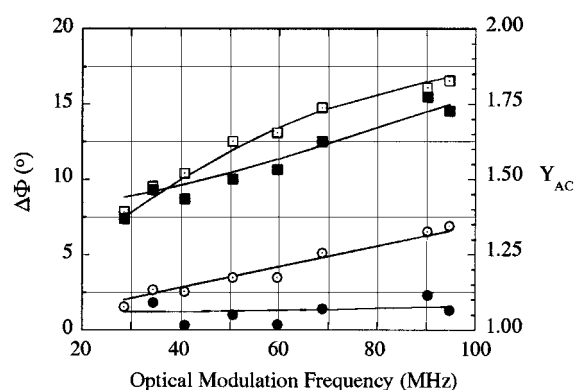


FIGURE 4 Multi-frequency rFLIM of fluorescein solutions containing 10% and 70% glycerol. Values denote the image (population) average of the respective images (adjacent cuvettes). Circles, 10% glycerol; squares, 70% glycerol. Open symbols,  $\Delta\Phi$ ; closed symbols,  $Y_{AC}$ . The solid lines represent global fits to the combined  $\Delta\Phi$  and  $Y_{AC}$  data, according to an isotropic rotator (Eqs. 7 and 8,  $r_{\infty} = 0$ ). The objective was Plan  $2\times$  air (NA 0.06). See text for a discussion of the results.

### Multi-frequency rFLIM measurements of fluorescein–glycerol solutions

Single frequency measurements can provide an indication of photophysical (and thus compositional) heterogeneity of a sample by comparison of apparent isotropic rotational correlation times derived from phase and modulation measurements. The quantitative resolution of multiple decaying components, in general, requires multi-frequency measurements. We questioned whether the homogenous rotational dynamics of fluorescein inferred by single-frequency analysis would also hold under the more stringent multi-frequency approach. To illustrate this capability for rFLIM measurements the mean  $\Delta\Phi$  and  $Y_{AC}$  values of spatially resolved images corresponding to two cuvettes containing fluorescein solutions in 10% and 70% glycerol, respectively, were measured at different modulation frequencies (Fig. 4). The two solutions were clearly distinguished by both parameters. The data were directly fitted to Eqs. 7 and 8 using weighted least-squares minimization (Excel, Microsoft Corp., Seattle, WA) of the sum of the squared differences between calculated and measured values of the four data sets;  $Y_{AC}$  was assigned an additional weighting factor of 100 relative to  $\Delta\Phi$ .

Global analyses were performed on the four data sets, using fixed lifetimes of 4.1 and 3.7 ns (10% glycerol and 70% glycerol, respectively), a linked (but free)  $r_o$  and an individually variable  $\phi$ ;  $r_{\infty}$  was set to 0 (isotropic rotator). The composite data from the two cuvettes fit using Eqs. 7 and 8 were described by a global  $r_o$  of 0.35 and  $\phi$  values of 0.23 and 1.82 ns for the 10% and 70% glycerol solutions, respectively (Fig. 4, solid lines). Similar parameters were obtained using commercial software (Globals Unlimited, Laboratory for Fluorescence Dynamics, Urbana-Champaign, IL, [ $r_o$  of 0.34 {95% confidence interval: 0.24–0.47}

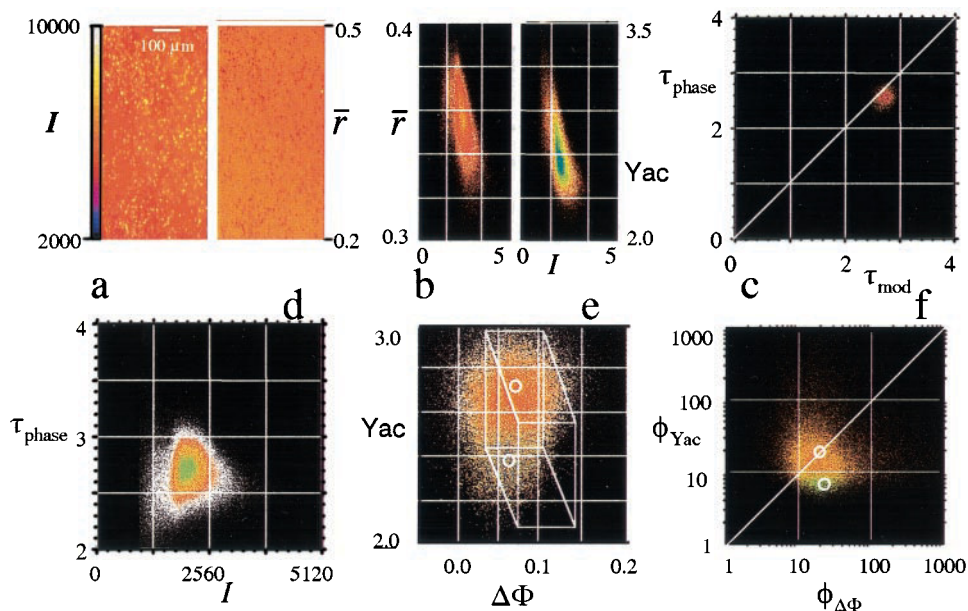


FIGURE 5 FLIM-rFLIM images and derived parameter histograms for EGFP in *E. coli* bacteria and free in solution. (a) wide-field intensity ( $I$ , left) and steady-state anisotropy ( $\bar{r}$ , right) images of the same selected field. (b) 2D histograms:  $\bar{r}$  versus  $I$ , left;  $Y_{AC}$  versus  $I$ , right. (c) 2D ( $\tau_{\text{phase}}$  versus  $\tau_{\text{mod}}$ ) histogram of bacterial subpopulation (masked by thresholding). (d) 2D ( $\tau_{\text{phase}}$  versus  $I$ ) histogram. (e) 2D ( $Y_{AC}$  versus  $\Delta\Phi$ ) histogram of free extracellular EGFP (upper cloud) and masked bacteria (lower cloud). Circles, mean values; solid lines, range of values predicted for EGFP as an isotropic rotator undergoing emFRET as a function of concentration (see text for details). (f) 2D ( $\phi_{Y_{AC}}$  versus  $\phi_{\Delta\Phi}$ ) histogram of free extracellular EGFP (upper orange cloud) and masked bacteria (lower green cloud). Circles, mean values calculated from the mean values of (e).  $\tau$  and  $\phi$  values in ns; intensities in arbitrary units;  $\Delta\Phi$  in radians. The objective was a Nikon 20 $\times$  (NA 0.5) Plan Air.

and  $\phi$  values of 0.20 ns {95% confidence interval: 0.09–0.34 ns} and 1.84 ns {95% confidence interval: 1.2–2.9 ns} for the 10% and 70% glycerol solutions, respectively]. The fits were not improved significantly by inclusion of more fit parameters (e.g.,  $r_{\infty}$ ). The predicted  $\phi$  value for the 70% glycerol solution (extrapolated from water, 1 cP, 0.1 ns; Periasamy and Verkman, 1992) was 2.1 ns and in agreement with the 95% confidence range. The results of the global analysis were in good agreement with the single-frequency data, confirming that fluorescein behaves as an isotropic rotator, a conclusion also derived in previous high-resolution time-resolved studies of fluorescein analogs (Fleming et al., 1976; Porter et al., 1977).

### Imaging rotational dynamics and emFRET in bacteria expressing EGFP

The family of green fluorescent proteins (GFPs) is used extensively in cell biology to assess the expression level and association of target proteins to which they are fused (Miyawaki and Tsien, 2000). They are characterized by relatively small Stokes shifts and correspondingly large Förster distances ( $R_0$ ) for homotransfer (Patterson et al., 2000), making them favorable for emFRET in rFLIM imaging experiments.

We questioned whether the phenomenon of emFRET would be observed in bacteria-expressing GFP due to the

high local concentration of the protein. To test this hypothesis, rFLIM images of EGFP-expressing bacteria were recorded (Fig. 5). Intense fluorescence was observed from the individual bacteria (Fig. 5 a, left; small dots at the resolution used in the experiment) above a weaker fluorescent background. The corresponding anisotropy image (Fig. 5 a, right) showed that the fluorescence anisotropy in the bacteria was lower than that of the free EGFP in the surrounding medium. This relationship was also reflected in the 2D histogram of  $\bar{r}$  versus  $I$  (Fig. 5 b, left) and of  $Y_{AC}$  versus  $I$  (Fig. 5 b, right), which revealed an inverse correlation consistent with a concentration-dependent depolarization within the bacteria, absent in the case of extracellular EGFP.

We attribute this effect to the existence of emFRET within the bacteria and rule out other possible interpretations. Depolarization due to changes in the electronic environment of the fluorophore or protein denaturation were excluded inasmuch as the fluorescence lifetime of EGFP in the bacteria (2.6 ns) was similar to that of the protein in solution (Fig. 5 c) and the distribution of lifetime values was uncorrelated to the intensity distribution (Fig. 5 d). Depolarization by reabsorption was also excluded in view of the bacterial dimensions (<10  $\mu$ ), limiting the maximal internal absorbance to <0.01 (based on calculations below).

Rotational depolarization could be rejected as the source of the lower intracellular steady-state anisotropy. The bacteria-associated fluorescence was segmented from the free

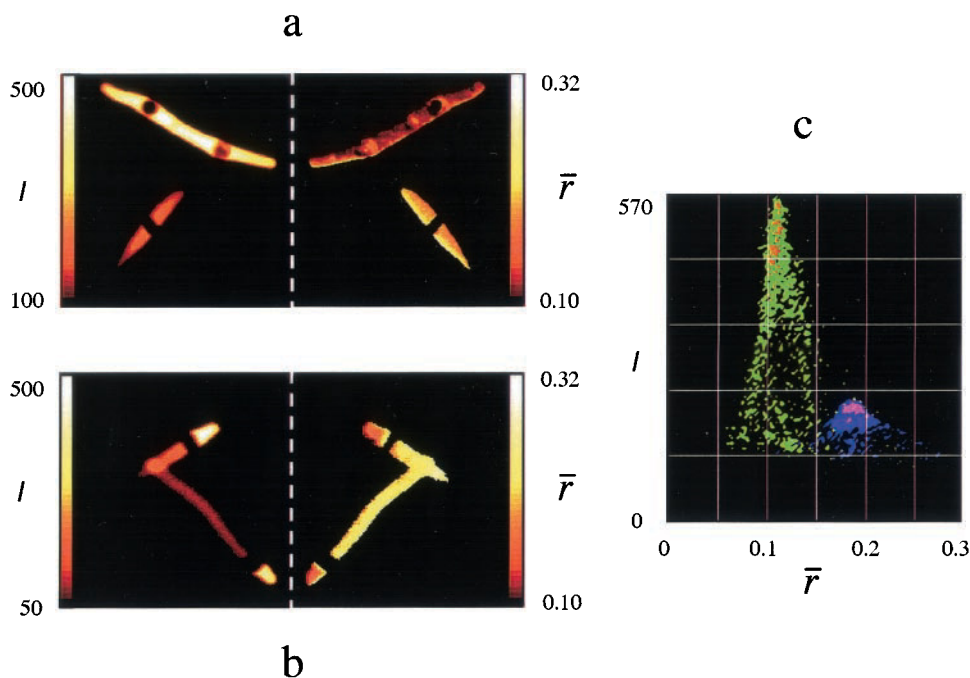


FIGURE 6 Confocal laser scanning microscope images of isolated *E. coli* bacteria expressing EGFP and demonstration of emFRET by anisotropy enhancement after photobleaching. (a) Intensity (left) and  $\bar{r}$  (right) of bacteria expressing different levels of EGFP. (b) Intensity (left) and  $\bar{r}$  (right) of bacteria after local photobleaching of the main cell body. For compactness of presentation, the intensity and anisotropy images were merged as mirror images. (c) 2D ( $\bar{r}$  versus  $I$ ) histogram of the image depicted in (b). The objective was a Zeiss 63 $\times$  (NA 1.2) C-Apochromat water immersion.

EGFP background by thresholding. The different anisotropy decays of the free and intracellular EGFP are reflected in the 2D histogram derived from the amplitude and modulation data (Fig. 5 e). For the free EGFP, the anisotropy decay reflected a homogeneous mode of rotational relaxation as deduced from the good agreement between the modulation and phase-derived isotropic rotational correlation times ( $\phi_{\Delta\Phi}$ ,  $\phi_{Y_{AC}}$ ; Eqs. 14 and 18,  $r_o = 0.39$ ; Fig. 5 f). The mean values of 19–20 ns were consistent with other measurements of GFPs (including EGFP) in solution (Partikian et al., 1998; Volkmer et al., 2000; Heikal et al., 2001). In contrast,  $\Delta\Phi$  and  $Y_{AC}$  differed for intracellular EGFP (mean values,  $\Delta\Phi = 0.057$  rad,  $Y_{AC} = 2.38$ ) and extracellular EGFP in solution ( $\Delta\Phi = 0.064$  rad,  $Y_{AC} = 2.72$ ), yielding apparent isotropic rotational correlation times, according to the formalism of Eqs. 14 and 18, of 22 and 7–8 ns, respectively (Fig. 5 f). This observation rules out simple differences in microviscosity as the underlying phenomenon, because in this case both  $\phi$  values would have been equally affected. Moreover, because a 16–20-ns  $\phi$  is characteristic for the free rotational diffusion of GFPs (Volkmer et al., 2000; Heikal et al., 2001), the lower value derived from the modulation data could only arise from another concentration-dependent depolarization mechanism operating in the intracellular milieu, i.e., emFRET.

Quantitative validation of this inference was made by applying the expanded rFLIM formalism, with which we simulated a ( $\Delta\Phi$ ,  $Y_{AC}$ ,  $c$ ) domain (indicated in Fig. 5 e as an

oblique parallelepiped bounded by white edges) with the  $c$  axis normal to the surface. Most of the measured data points were accommodated, using the parameter set  $r_o = 0.39$ ,  $\tau = 2.6$  ns,  $\phi = 19$  ns,  $\alpha c = 0-0.25$ , the apparent  $R_o$  for emFRET of 7.3 nm obtained from the calibration of Fig. 7 (see below), and added random noise ( $\Delta\Phi$  standard deviation = 0.02;  $Y_{AC}$  CV = 0.05, values close to those observed for intracellular EGFP). As expected, the values for free EGFP lie in the upper (posterior) rectangular face corresponding to  $c = 0$  (no emFRET). The lower (anterior) rectangular face corresponds to the highest simulated EGFP concentration (0.25 mM) and reflects the expected influence of emFRET on the rFLIM parameters (higher  $\Delta\Phi$ , lower  $Y_{AC}$ ). The data for intracellular EGFP appear to fall in a region of intermediate concentration. A direct albeit rough estimate (0.6 mM) of the mean intracellular EGFP concentration was derived for a bacterial suspension similar to the one from which the sample depicted in Fig. 6 was drawn. The calculation was based on the volume fraction of filtered bacteria (0.15%), the mean EGFP concentration of the bacterial suspension (0.7  $\mu$ M) computed from its fluorescence (after washing to remove extracellular material) relative to that of a standard solution, and the  $\sim 75\%$  water content of *E. coli* (Davis et al., 1973).

Higher resolution images of the EGFP-expressing bacteria were acquired with a confocal laser scanning microscope adapted for steady-state anisotropy measurements (Fig. 6). The bacteria were unusually long and displayed a homoge-

neous (yet variable from cell to cell) intense fluorescence from the expressed EGFP with a reduction in the region of the nucleoid, presumably due to (partial) exclusion, and complete absence from septa demarcating the cell body from prevalent terminal buds. The latter were also abundant as isolated suspended structures. The steady-state anisotropy images of the individual bacterial cells were rather uniform with characteristically low values, in some cells even  $<0.2$ . There was a notable inverse correlation between intensity and anisotropy within the cellular population. This relationship was established over a greater range by subjecting the bacteria to local photobleaching, achieved via exposure to the intense 488-nm beam of the external laser (Fig. 6 *b*). Reequilibration by translational diffusion within the bacteria was very rapid, i.e., beyond the temporal resolution of the scanning microscope. The function of the transverse septa as diffusion barriers was established by the observation that the terminal buds were not depleted of fluorescence after photobleaching the distal segments of the adjoined cell (Fig. 6 *b*). In addition, the 2D histogram of the bacterial data clearly established the inverse correlation between  $\bar{r}$  and  $I$  (Fig. 6 *c*). Upon extended photobleaching, the post-bleach  $\bar{r}$  values increased to the range (0.30–0.34) characteristic for free EGFP.

From these experiments, we attribute the lower anisotropy of the intracellular EGFP to classical concentration depolarization, i.e., emFRET. This phenomenon had not been previously reported for free GFPs in solution.

We confirmed the existence of emFRET by direct measurements of EGFP solutions in a spectrofluorimeter (Fig. 7). The emFRET formalism predicts a lack of quenching (the intensity should be linear with concentration in the absence of protein oligomerization) but a progressive depolarization (in accordance with Eq. 30) as one increases the fluorophore concentration. Both these conditions were observed (Fig. 7). A fit of the  $\bar{r}$  versus  $c$  data (excluding the highest point, see below) to Eq. 30 yielded  $r_o/(1 + \sigma) = 0.32$  and  $\beta = 0.49 \pm 0.02 \text{ mM}^{-1}$ . Using  $\sigma = 0.14$  ( $\tau = 2.6$  ns;  $\phi = 19$  ns) and Eq. 31, we obtained  $\alpha = 1.05 \pm 0.05 \text{ mM}^{-1}$ ,  $r_o = 0.36$  and an apparent  $R_o$  of  $7.3 \pm 0.1$  nm. The latter value greatly exceeds the reported  $R_o$  for emFRET of EGFP, based on the spectral overlap integral (4.7 nm; Patterson et al., 2000). That is, the concentration-dependent depolarization was much greater than expected, an observation we tentatively attribute to the complex photophysical properties of GFPs (and EGFP in particular, Heikal et al., 2001; Cotlet et al., 2001). We will develop this point further elsewhere but note in passing that the spectral distribution of  $\bar{r}$  demonstrated larger values for wavelengths  $<510$  nm, i.e., to the blue side of the emission peak, and a distinct, albeit weak, dependence on the excitation wavelength.

One could conceive of an alternative explanation for the unexpectedly extensive depolarization based on potential emFRET-enhancing association (e.g., dimerization) of EGFP. However, the lack of a systematic deviation from the

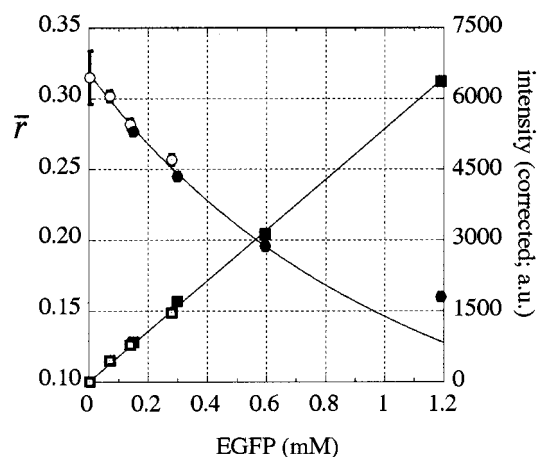


FIGURE 7 Concentration depolarization (emFRET) of EGFP solutions. Solutions were measured in microcuvettes (pathlength 0.25 mm) at 20°C. Values of  $\bar{r}$  (circles) averaged over the emission range 520–560 nm and intensities (squares) corrected for inner filter effects on excitation, see Experimental) plotted as a function of EGFP concentration. The  $\bar{r}$  values (for  $c < 1$  mM) were fit to Eq. 30 (—; see text in Results and Discussion) and the corrected  $I$  values were fit to a straight line. Data were taken in two separate experiments (denoted by the open and closed symbols; allowance was made for a systematic difference of 15% in the signal levels of the two data sets).

functional concentration dependence of Eq. 30 in the range  $<1$  mM excludes this eventuality. We attribute the failure of the  $\bar{r}$  value for 1.2 mM to conform with the fit to the lower concentration data to possible measurement error (related to the high absorbance), the limitations of the formalism used for data analysis (Eq. 30), and possible/probable size exclusion effects due to the large molecular mass of EGFP. We know of no comparable protein system exhibiting emFRET for which quantitative data have been reported in the literature.

The parameters determined from the in vitro measurements were in excellent agreement with the bacterial data. The upper concentration of 0.25 mM inferred from the wide-field rFLIM measurements is consistent with the value deduced from the change in anisotropy (Fig. 5 *b*) and the calibration of Fig. 7. From the pre- and post-bleach  $\bar{r}$  values of Fig. 6 *b*, and the calibration of Fig. 7, we estimated pre- and post-bleach intracellular EGFP concentrations of 1.3 and 0.55 mM, respectively. According to the same procedure, the concentrations in the high- and low-expression cells of Fig. 6 *a* were 1.3 and 0.2 mM. In both cases, the relative levels derived from  $\bar{r}$  agreed well with those computed from the fractional intensities.

## DISCUSSION

The primary advantage of rFLIM lies in its ability to characterize and discriminate heterogeneity resulting from com-

plex diffusional dynamics at the molecular and cellular level. This entails two main requirements:

(i) *Spatial resolution of fluorescence anisotropy decay (cellular level) and the ability to detect or resolve multiple decay components (molecular level) within an arbitrary spatial region of interest.* Using a model system, we demonstrated that this information can be extracted on a pixel-by-pixel basis by combining the steady-state images (intensity and DC polarization ratio) with the modulated images (lifetime, phase shift, and AC polarized ratio) obtained by rFLIM/FLIM at a single modulation frequency. This method of analysis was validated with multi-frequency rFLIM measurements of fluorescein in solution and used to detect rotation and concentration depolarization of EGFP in bacteria. The data were obtained in parallel for all image elements in a wide-field optical configuration, providing an efficient means of assessing molecular dynamics within and across entire cells. In this sense, the rFLIM approach featured in this paper differs from single-point anisotropy decay measurements (Verkman et al., 1990; Tramier et al., 2000) or methods based on scanning systems (Buehler et al., 2000; Dyba et al., 2000) to acquire a polarization decay image. rFLIM can be considered complementary to the other existing methods for quantitative imaging of molecular states and environments.

Several potential sources of error in both experiment and analysis need to be considered in applying the rFLIM technique. Depolarization introduced by high-aperture objectives has been reported by others and should be taken into account either empirically (Fushimi et al., 1990) or by an analysis procedure using a mathematical model (Axelrod, 1979, 1989; Florine-Casteel, 1990; Bahlmann and Hell, 2000; Tramier et al., 2000). For the samples used in this report, a first-order correction for the biases in the detection of the two polarized emission components was used (Dix and Verkman, 1990). This approach seemed reasonable inasmuch as the numerical aperture of the lenses was generally kept low and, for the solutions, appeared to influence the polarization ratios only slightly, with no measurable effect on the phase shift. However, other procedures may be required under different circumstances, e.g., for high-NA imaging of cellular samples or when a significant fraction of fluorophores (Subramaniam et al., 2002) have its transition moments aligned parallel to the optic axis (Axelrod, 1989; Florine-Casteel, 1990; Fushimi et al., 1990).

(ii) *Consideration of the effects of measurement statistics.* In a previous study of conventional lifetime images, we noted that random errors among lifetime images and within a single lifetime image are dominated by different factors (Hanley et al., 2001). rFLIM images have a number of unique characteristics compared to conventional FLIM images that need to be taken into account. First, the rFLIM parameters obtained from the measurement scheme described here represent the combined results of multiple data sets; the unpolarized lifetime and the parallel and perpen-

dicular phase and amplitudes. Second, propagation of noise in Eqs. 1–27 is far more complicated than in conventional FLIM. Error propagation effects are particularly problematic when the mean of the measured parameter is close to the physical limits, e.g., of  $\Delta\Phi$  ( $0, \Delta\Phi_{\max}$ ). Under certain conditions, detector noise can broaden part of the distribution into a nonphysical parameter space, leading to truncation of parts of the computed distributions. One would anticipate that this problem could be circumvented by several methods: by adjustment of experimental variables, especially the modulation frequency; by averaging the raw data over a predetermined region of interest (at the expense of spatial resolution); or by the judicious combined use of experimental variables in the analysis, as demonstrated for  $\Delta\Phi$  and  $\bar{\tau}$  in this work. We would emphasize the importance of applying appropriate image-analysis procedures to instrumental parameters such as the  $G$ -factor (Eq. 4), which is expected to vary systematically but only gradually over the image. Preliminary efforts indicate that significant improvements in the statistical distributions of derived parameters can be achieved (Table 2). Data smoothing and other sophisticated filtering operations can also be performed on the raw data. The images presented in this paper were unsmoothed.

Third, when working with image data, the large number of replicate measurements represented by the many pixels in the image lead to distributions with very precisely defined means. The ability to discriminate two spatially distinct normal distributions of parameters is borne out by Student's  $t$ -test. For two regions, each with 1000 pixels, and a standard deviation in rotational correlation time of 0.5 ns, one should, in principle, be able to discriminate differences in mean rotational correlation times of 37 ps at the 99% confidence interval. The advantage of a parallel imaging arrangement is that instrumental and environmental factors such as temperature variations or fluctuations in laser power affect all pixels equally. This does not necessarily apply to methods that use serial acquisition.

A related question is whether observed heterogeneity in a given sample reflects inherent heterogeneity in the local chemical or physical microenvironment, or primarily measurement statistics and detector noise (despite a uniform population of molecules). A lack of spatial correlation among different independent parameters (e.g., those represented in Eq. 3) constitutes evidence for spatial macroscopic homogeneity within each volume element encompassed by each pixel. The cuvette solution experiments illustrated the measured noise and propagated error levels anticipated for a homogenous population of fluorophores. Comparison of computed correlation time histograms derived from different independent parameters or from combination of parameters in the analysis procedure offers a first-order approach for detecting the presence of multiple correlation times, i.e., heterogeneity at the microscopic level. The inspection of various 2D histograms may provide a simple means for

detecting regions that are homogenous (or inhomogeneous) in rotational correlation time space in cellular systems, as has been demonstrated here for the first time. Related approaches have been successful in multiparameter image cytometry (Demandolx and Davoust, 1997a,b). An alternative approach is to define regions of interest based on an independent fluorescence parameter or subcellular structures and use population means to evaluate the anisotropy decay properties. To a certain extent, this procedure may eliminate some of the noise-propagation problem but, of course, at the sacrifice of spatial resolution.

The raw parameters obtained from rFLIM measurements by themselves provide an image contrast and can be analyzed with any model of arbitrary complexity to gain increased photophysical insight. Here, single-frequency rFLIM data were analyzed in terms of the isotropic rotator or hindered rotator models, for which we have presented a comprehensive formal description. These models allow the determination of only a single rotational correlation time per pixel and hence are limited in the number of anisotropy decay modes they can resolve. This problem also exists in the context of single-frequency FLIM where apparent fluorescence lifetimes ( $\tau_{\text{phase}}$ ,  $\tau_{\text{mod}}$ ) are obtained. However, it is worth considering the information content of single-frequency measurements, because these are the easiest to obtain and analyze. The computed  $\phi$ ,  $r_0$ , and  $r_\infty$  values of the hindered rotator model can provide useful information about the mean rate and extent of fluorophore fluctuations (Kinosita et al., 1982). These considerations are important in view of the subnanosecond–nanosecond backbone fluctuations of proteins (Gangal et al., 1998; Clore et al., 1990; Vergani et al., 2000); precisely these timescales are accessible by MHz rFLIM. The general applicability of the hindered rotator model is exemplified by numerous studies of fluorescence membrane probes in membrane systems (Wieb van der Meer, 1993), in analyzing fluctuations of enzyme–fluorophore complexes in solution (Chang et al., 1983; Cross and Fleming, 1986) and of fluorescein-labeled ligand–receptor pair dynamics during receptor internalization in cells (Martin-Fernandez et al., 1998). The  $r_\infty$  parameter may also be useful in the event that it reflects bound states of fluorescent probes in cellular systems. For example, certain dyes used as microviscosity probes can give misleading results if they bind to (but not partition into) the cellular compartment of interest (Partikian et al., 1998). A nonzero value of  $r_\infty$  indicates that care should be taken in interpreting steady-state anisotropy results solely in terms of changes in microviscosity or in the hydrodynamic volume of the rotating unit.

### emFRET of EGFP

Thus far, we have considered diffusional sources of fluorescence depolarization, i.e., the effect of molecular reorientation of the fluorophore during its excited-state lifetime.

However, fluorescence anisotropy can also reflect the proximity or surface density of labeled cell constituents, for example, via the homotransfer of electronic energy (emFRET). The results and analysis presented here showed that EGFP can undergo emFRET at the concentrations achieved in bacteria expressing this protein. In contrast, EGFP released into the medium from lysed bacteria exhibited the rotational relaxation parameters characteristic of the free monomeric molecule. rFLIM was required to distinguish between concentration depolarization and rotational diffusion as the cause of the intracellular depolarization. For isotropic rotators, the apparent rotational correlation times derived from phase and modulation using the classical formalism for frequency domain analysis are equal. In the presence of concentration depolarization emFRET, these quantities are perturbed systematically to an extent that can be accounted for by the expanded formalism developed in the course of this investigation. In addition, the comparison and correlation of various parameters (intensity, lifetime) within an image of a large population of cells allow alternative mechanisms of depolarization to be tested and discarded. Conventional FRET among different molecules (donor–acceptor) also exhibits an anisotropy signature (increase of donor anisotropy, decrease of acceptor anisotropy). Finally, as noted by Matayoshi and Swift (2000) the complementarity of fluorescence anisotropy to other techniques, such as fluorescence correlation spectroscopy, makes it a powerful tool in examining protein–ligand interactions.

The demonstration of pronounced emFRET in EGFP constitutes, to our knowledge, a new finding for the important family of visible fluorescent proteins and one that has two important implications. 1) In studies based on heterotransfer FRET, i.e., between dissimilar GFPs, the intervention of emFRET with each member of the donor–acceptor pair has to be considered. That is, there exists a potential for a greater spatial dissemination of the excitation energy, which has implications for the molecular interpretation of the data. 2) In evaluating the yield of EGFP fusion proteins in bacteria, emFRET, i.e., the measurement of anisotropy, offers the potential for a much easier and more reliable determination of concentration and thus of yield, in contrast to intensity measurements that require nontrivial calibrations of fluorescence signals, and of cell number and size. The anisotropy determinations can be readily performed on cellular suspensions. Furthermore, in the imaging context, fluorescence intensities vary greatly due to the combined effects of distribution (pathlength) and depth of focus, whereas anisotropy values are relatively insensitive to these issues (Fig. 6 c). It is interesting that the high intracellular concentrations of EGFP achieved in the bacterial cultures, accounting for a significant fraction of total protein, led to such pronounced phenotypic effects reflected in the unusual morphology and budding tendency of the expressing *E. coli* cells. We are currently exploiting the phenomenon of em-

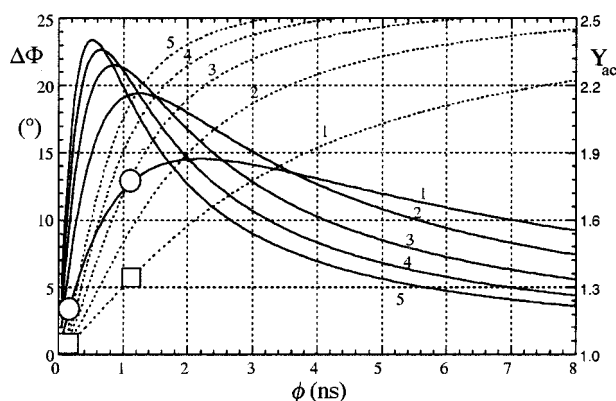


FIGURE A1 Dependence of  $\Delta\Phi$  (—) and  $Y_{AC}$  (---) on  $\phi$  and  $\omega\tau$ . Isotropic rotator: optical modulation frequency =  $58 \cdot \gamma$  MHz,  $\tau = 4.2$  ns,  $r_o = 0.35$ ,  $r_\infty = 0$ . The numbers identifying the curves are =  $\gamma$ . The circles and squares correspond closely to the experimental system (fluorescein in 10% and 61% glycerol solutions) studied by rFLIM (Fig. 3, Table 2).

FRET in studies of GFP fusion proteins involved in signal transduction mediated by receptor tyrosine kinases.

### Extensions of rFLIM

We can anticipate a number of technical extensions to the rFLIM technique, some of which were recently introduced in FLIM. These include the use of multiple frequencies in parallel (Squire et al., 2000) to investigate more complex anisotropy decay models, the global analysis of image data (Verveer et al., 2000), the extension of the rFLIM formalism to account for multiple species, including those arising in FRET, and the direct determination of  $\Delta\Phi$ . The latter feature was one of the prime motivations in the original development of the differential phase technique for solution measurements (Weber, 1977, 1978).

### APPENDIX: SIMULATIONS OF FREQUENCY-DOMAIN ANISOTROPY PARAMETERS

To illustrate the theory and examine effects of error propagation, we present simulations of the anisotropy decay parameters under conditions that closely mimic those used in our experiments. Computations of  $\Delta\Phi$  and  $Y_{AC}$  as a function of the rotational correlation time  $\phi$  for an isotropic rotator (optical modulation frequency = 58 MHz,  $\tau = 4.2$  ns,  $r_o = 0.35$ ,  $r_\infty = 0$ ), are shown in Fig. A1 over a range corresponding to  $\sigma = 0.5$ – $\infty$ . These conditions were selected because they matched closely those used in experiments on fluorescein solutions in glycerol (see Experimental Results). For a detection uncertainty in  $\Delta\Phi$  of  $\sim 2^\circ$  and in  $Y_{AC}$  of  $\sim 0.05$ , a  $\phi$  in the range  $\approx 0.1$ –10 ns (possibly higher) should be resolvable. We note again the monotonic behavior of  $Y_{AC}$  as opposed to the bell-shaped function  $\Delta\Phi$ . The latter exhibits two possible solutions of  $\phi$  for any given value of the phase-shift. However, combination with  $Y_{AC}$  and use of various frequencies can eliminate the ambiguity. Note in Fig. A1 the reversal in the order of the frequency-dependent  $\Delta\Phi$  curves about the peak.

A second issue relates to error propagation, particularly in the case of  $\Delta\Phi$ -derived parameters. The restrictions imposed by the theoretical upper bound of  $\Delta\Phi$  on the solution of  $\phi_{\Delta\Phi}$  (see text) can lead to rejection of

experimental values, thereby skewing the distribution of  $\phi_{\Delta\Phi}$  derived from image data. We simulated in Fig. A2 the effect of changing the mean and width of a Gaussian distribution of  $\Delta\Phi$  on the computed  $\phi_{\Delta\Phi}$  distribution. It is apparent that the width, and the degree and direction of asymmetry of the  $\phi_{\Delta\Phi}$  distributions were greater for the 0.22 radian ( $12.6^\circ$ , corresponding to a  $\phi_{\Delta\Phi}$  of 1.1 ns) distribution than for the 0.05 radian ( $2.9^\circ$ , corresponding to a  $\phi_{\Delta\Phi}$  of 0.14 ns) distribution, in the case of the selected standard deviations of  $\Delta\Phi$  (0.005 and 0.05). The broadening of the 0.22 radian  $\Delta\Phi$  data also caused 23% of the values to become nonphysical, in accordance with Eq. 12, which, for the given parameters (optical modulation at 58 MHz,  $\tau = 4.2$  ns,  $r_o = 0.35$ ,  $r_\infty = 0$ ), yielded a  $\Delta\Phi_{\max} = 0.26$  radians (corresponding to a  $\phi_{\Delta\Phi}$  of 1.9 ns). Thus, the postulated  $\Delta\Phi$  distribution did not (could not) map completely to a distribution of physically realizable  $\phi_{\Delta\Phi}$  values. The effect of varying the standard deviation (expressed as the CV) of the two  $\Delta\Phi$  distributions on the computed mean  $\phi_{\Delta\Phi}$  and the corresponding CVs is shown in Fig. A2, B and C. The rotational correlation time decreased as the CV increased for the 0.22 radian case (Fig. A2 C) due to the exclusion of imaginary values arising for CVs of  $\Delta\Phi > 0.005$ , whereas a slight increase was observed for the 0.05 radian case (Fig. A2 B). This increase reflects the inherent lack of congruence between distributions of  $\Delta\Phi$  and  $\phi_{\Delta\Phi}$ , and was also evident initially in the plot of the 0.22 radian distribution. However, the CV of  $\phi_{\Delta\Phi}$  was generally proportional (and nearly equal) to that of  $\Delta\Phi$ . The fluctuations observed in Fig. A2, B and C are representative for the sampling size (1000 points) used in the simulations.

We dedicate this publication to the memory of Gregorio Weber, the originator of most concepts and experimental approaches for the study of rotational diffusion in biological systems based on fluorescence.

A.H.A.C. and V.S. were recipients of a long-term postdoctoral fellowship from The Human Frontier Science Program.

### REFERENCES

- Albrecht, A. C. 1961. Polarizations and assignments of transitions: the method of photoselection. *J. Mol. Spec.* 6:84–108.
- Axelrod, D. 1979. Carbocyanine dye orientation in red cell membrane studied by microscopic fluorescence polarisation. *Biophys. J.* 26: 557–573.
- Axelrod, D. 1989. Fluorescence polarisation microscopy. *Methods Cell. Biol.* 30:333–352.
- Bahlmann, K., and S. W. Hell. 2000. Depolarization by high aperture focusing. *Appl. Phys. Lett.* 77:612–614.
- Bene, L., M. J. Fulwyler, and S. Damjanovich. 2000. Detection of receptor clustering by flow cytometric fluorescence anisotropy measurements. *Cytometry.* 40:292–306.
- Blackman, S. M., D. W. Piston, and A. H. Beth. 1998. Oligomeric state of human erythrocyte Band 3 measured by fluorescence resonance energy homotransfer. *Biophys. J.* 75:1117–1130.
- Bojarski, C., and K. Sienicki. 1989. Energy transfer and migration in fluorescent solutions. In *Photochemistry and Photophysics*, Vol I. J. F. Rabek, P. F. editor. CRC Press, Boca Raton, FL. 1–57.
- Buehler, C., C. Y. Dong, P. T. O. So, T. French, and E. Gratton. 2000. Time-resolved polarization imaging by pump-probe (stimulated emission) fluorescence microscopy. *Biophys. J.* 79:536–549.
- Chang, M. C., A. J. Cross, and G. R. Fleming. 1983. Internal dynamics and overall motion of lysozyme studied by fluorescence depolarization of the eosin lysozyme complex. *J. Biomol. Struct. Dynam.* 1:299–319.
- Clare, G. M., P. C. Driscoll, P. T. Wingfield, and A. M. Gronenborn. 1990. Analysis of the backbone dynamics of interleukin-1-beta using two-dimensional inverse detected heteronuclear N-15 H-1 NMR spectroscopy. *Biochemistry.* 29:7387–7401.
- Cole, M. J., J. Siegel, S. E. D. Webb, R. Jones, K. Dowling, P. M. W. French, M. J. Lever, L. O. D. Sucharov, M. A. A. Neil, R. Juskaitis, and

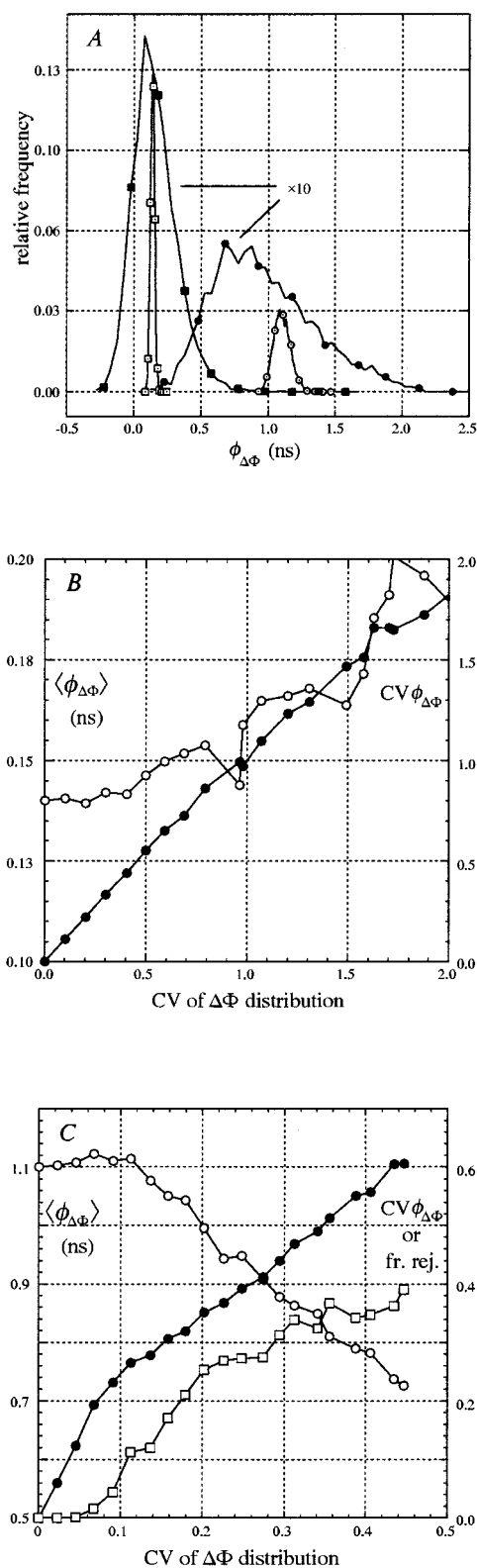


FIGURE A2 Simulations illustrating the influence of Gaussian distributions of  $\Delta\Phi$  values on  $\phi_{\Delta\Phi}$  distributions for an isotropic rotator (optical modulation frequency = 58 MHz,  $\tau = 4.2$  ns,  $r_o = 0.35$ ,  $r_\infty = 0$ ). (A) Histograms corresponding to a mean  $\Delta\Phi$  of 0.05 radians (corresponding to a  $\phi$  of 0.14 ns, left curves: squares) and 0.22 radians (corresponding to a

T. Wilson. 2000. Whole-field optically sectioned fluorescence lifetime imaging. *Opt. Lett.* 25:1361–1363.

Cotlet, M., J. Hofkens, M. Maus, T. Gensch, M. Van der Auweraer, J. Michiels, G. Dirix, M. Van Guyse, J. Vanderleyden, A. J. W. G. Visser, and F. C. De Schryver. 2001. Excited-state dynamics in the enhanced green fluorescent protein mutant probed by picosecond time-resolved single photon counting spectroscopy. *J. Phys. Chem. B.* 105:4996–5006.

Cross, A. J., and G. R. Fleming. 1986. Influence of inhibitor binding on the internal motions of lysozyme. *Biophys. J.* 50:507–512.

Davis, B., R. Dulbecco, H. N. Eisen, H. S. Ginsberg, and W. B. Wood. 1973. *Microbiology*. Harper and Row, Publishers, Inc., New York.

Demandolx, D., and J. Davoust. 1997a. Multiparameter image cytometry: from confocal micrographs to subcellular fluorograms. *Bioimaging*. 5:159–169.

Demandolx, D., and J. Davoust. 1997b. Multicolour analysis and local image correlation in confocal microscopy. *J. Microsc.* 185:21–36.

Dix, J. A., and A. S. Verkman. 1990. Mapping of fluorescence anisotropy in living cells by ratio imaging. *Biophys. J.* 57:231–240.

Dyba, M., T. A. Klar, S. Jakobs, and S. W. Hell. 2000. Ultrafast dynamics microscopy. *Appl. Phys. Lett.* 77:597–599.

Engstrom, S., M. Lindberg, and L. B.-A. Johansson. 1992. Fluorescence anisotropy of rotating molecules in the presence of energy migration. *J. Chem. Phys.* 96:7528–7534.

Fleming, G. R., J. M. Morris, and G. W. Robinson. 1976. Direct observation of rotational diffusion by picosecond spectroscopy. *Chem. Phys.* 17:91–100.

Florine-Casteel, K. 1990. Phospholipid order in gel- and fluid-phase cell-size liposomes measured by digitized video fluorescence polarization microscopy. *Biophys. J.* 57:1199–1215.

Fushimi, K., J. A. Dix, and A. S. Verkman. 1990. Cell-membrane fluidity in the intact kidney proximal tubule measured by orientation-independent fluorescence anisotropy imaging. *Biophys. J.* 57:241–254.

Gadella, T. W. J., Jr., T. M. Jovin, and R. M. Clegg. 1993. Fluorescence lifetime imaging microscopy (FLIM)-spatial-resolution of microstructures on the nanosecond time-scale. *Biophys. Chem.* 48:221–239.

Gangal, M., S. Cox, J. Lew, T. Clifford, S. M. Garrod, M. Aschbahr, S. S. Taylor, and D. A. Johnson. 1998. Backbone flexibility of five sites on the catalytic subunit of CAMP-dependent protein kinase in the open and closed conformations. *Biochemistry*. 37:13728–13735.

Gautier, I., M. Tramier, C. Durieux, J. Coppey, R. B. Pansu, J. C. Nicolas, K. Kemnitz, and M. Coppey-Moisan. 2001. Homo-FRET microscopy in living cells to measure monomer–dimer transition of GFP-tagged proteins. *Biophys. J.* 80:3000–3008.

Ghiggino, K. P., M. R. Harris, and P. G. Spizziri. 1992. Fluorescence lifetime measurement using a novel fibreoptic laser scanning confocal microscope. *Rev. Sci. Instrum.* 63:2999–3002.

Ha, T., T. A. Laurence, D. S. Chemla, S. Weiss. 1999. Polarization spectroscopy of single fluorescent molecules. *J. Phys. Chem.* 103: 6839–6850.

Hanley, Q. S., V. Subramaniam, D. J. Arndt-Jovin, and T. M. Jovin. 2001. Fluorescence lifetime imaging: multi-point calibration, minimum resolvable differences, and artifact suppression. *Cytometry*. 43:248–260.

$\phi$  of 1.1 ns, right curves: circles). The open symbols are for an SD of the  $\Delta\Phi$  distribution of 0.005 radians and the closed symbols for an SD of 0.05 radians. Each distribution was generated with 5000 points, of which 1238 were rejected (by virtue of yielding imaginary solutions of Eq. 14) from the 1.1-ns  $\phi$  histogram corresponding to the 0.05 SD  $\Delta\Phi$  distribution. Symbols are shown for every tenth point. (B) Effect of increasing the CV (at constant mean) of the  $\Delta\Phi$  distribution centered at 0.05 radians ( $\phi$  of 0.14 ns) on the computed mean  $\phi_{\Delta\Phi}$  (open circles) and the CV (closed circles) of the  $\phi_{\Delta\Phi}$  histogram. 1000 points were used for each calculation. (C) As in B but for the  $\Delta\Phi$  distribution centered at 0.22 radians ( $\phi$  of 1.1 ns). Open squares, fraction of rejected (imaginary) points.

- Heikal, A. A., S. T. Hess, and W. W. Webb. 2001. Multiphoton molecular spectroscopy and excited-state dynamics of enhanced green fluorescent protein (EGFP); acid-base specificity. *Chem. Phys.* 274:37–55.
- Jablonski, A. 1960. On the notion of the emission anisotropy. *Bull. Acad. Pol. Sci. C1.* 38:259–264.
- Jakobs, S., V. Subramaniam, A. Schonle, T. M. Jovin, and S. W. Hell. 2000. EGFP and DsRed expressing cultures of *Escherichia coli* imaged by confocal, two-photon and fluorescence lifetime microscopy. *FEBS Lett.* 479:131–135.
- Jameson, D. M., and T. L. Hazlett. 1986. Fluorescence investigations of the elongation factor TU system. In *Fluorescent Biomolecules*. D. M. Jameson and G. D. Reinhardt, editors. Plenum Press, New York and London. 61–86.
- Jameson, D. M., and W. H. Sawyer. 1995. Fluorescence anisotropy applied to biomolecular interactions. *Methods Enzymol.* 246:283–300.
- Jovin, T. 1979. Fluorescence polarization and energy transfer: theory and application. In *Flow Cytometry and Sorting*. M. R. Melamed, P. F. Mullaney, and M. L. Mendelsohn, editors. John Wiley and Sons, New York. 137–165.
- Kinosita, K., Jr., A. Ikegami, and S. Kawato. 1982. On the wobbling-in-cone analysis of fluorescence anisotropy decay. *Biophys. J.* 37:461–464.
- Lakowicz, J. R., F. G. Prendergast, and D. Hogen. 1979. Differential polarized phase fluorometric investigations of diphenylhexatriene in lipid bilayers. Quantitation of hindered depolarizing rotations. *Biochemistry.* 18:508–519.
- Lakowicz, J. R. 1983. Theory and application of differential polarized phase fluorometry. In *Time-Resolved Spectroscopy in Biochemistry and Biology*. R. B. Cundall and R. E. Dale, editors. NATO ASI series. vol 69. Plenum Press, New York. 541–554.
- Lakowicz, J. R., and A. Balter. 1982. Theory of phase-modulation fluorescence spectroscopy for excited-state processes. *Biophys. Chem.* 16: 99–115.
- Lakowicz, J. R., H. Szmazinski, K. Nowaczyk, K. W. Berndt, and M. Johnson. 1992. Fluorescence lifetime imaging. *Anal. Chem.* 202: 316–330.
- Lipari, G., and A. Szabo. 1980. Effect of librational motion on fluorescence depolarization and nuclear magnetic relaxation data in macromolecules and membranes. *Biophys. J.* 30:489–506.
- Magde, D., G. E. Rojas, and P. G. Seybold. 1999. Solvent dependence of the fluorescence lifetimes of xanthene dyes. *Photochem. Photobiol.* 70:737–744.
- Mantulin, W. W., and G. Weber. 1977. Rotational anisotropy and solvent-fluorophore bonds: an investigation by differential polarized phase fluorometry. *J. Chem. Phys.* 66:4092–4099.
- Martin-Fernandez, M. L., M. J. Tobin, D. T. Clarke, C. M. Gregory, and G. R. Jones. 1998. Subnanosecond polarised microfluorimetry in the time domain: an instrument for studying receptor trafficking in live cells. *Rev. Sci. Instr.* 69:540–543.
- Marriot, G., R. M. Clegg, D. J. Arndt-Jovin, and T. M. Jovin. 1991. Time resolved imaging microscopy-phosphorescence and delayed fluorescence imaging. *Biophys. J.* 60:1374–1387.
- Matayoshi, E., and K. Swift. 2001. Applications of FCS to protein–ligand interactions: comparison with fluorescence polarization. In *Fluorescence Correlation Spectroscopy*. F. P. Scafer, J. P. Toennies, W. Zinth, editors. Vol 65. Springer, Berlin/Heidelberg. 85–98.
- Miyawaki, A., and R. Y. Tsien. 2000. Monitoring protein conformation and interactions by fluorescence resonance energy transfer between mutants of green fluorescent protein. *Methods Enzymol.* 327:472–500.
- Periasamy, N., and A. S. Verkman. 1992. Subtraction of background fluorescence in multiharmonic frequency-domain fluorimetry. *Anal. Biochem.* 201:107–113.
- Partikian, A., B. Olveczky, R. Swaminathan, Y.-X. Li, and A. S. Verkman. 1998. Rapid diffusion of green fluorescent protein in the mitochondrial matrix. *J. Cell Biol.* 140:821–829.
- Patterson, G. H., S. M. Knobel, W. D. Sharif, S. R. Kain, and D. W. Piston. 1997. Use of the green fluorescent protein and its mutants in quantitative fluorescence microscopy. *Biophys. J.* 73:2782–2790.
- Patterson, G. H., D. W. Piston, and B. G. Barisas. 2000. Förster distances between green fluorescent protein pairs. *Anal. Biochem.* 284:438–440.
- Piston, D. W., D. R. Sandison, and W. W. Webb. 1992. Time-resolved fluorescence imaging and background rejection by two-photon excitation in laser-scanning microscopy. *SPIE Proc.* 1640:379–389.
- Porter, G., P. J. Sadkowski, and C. J. Treadle. 1977. Picosecond rotational diffusion in kinetic and steady-state fluorescence spectroscopy. *Chem. Phys. Letts.* 49:416–420.
- Schneider, P., and R. N. Clegg. 1997. Rapid acquisition, analysis and display of fluorescence lifetime-resolved images for real-time applications. *Rev. Sci. Instrum.* 68:4107–4119.
- Scully, A. D., R. B. Ostler, D. Phillips, P. O. O’Neil, K. M. S. Townsend, A. W. Parker, and A. J. MacRobert. 1997. Application of fluorescence lifetime imaging microscopy to the investigation of intracellular PDT mechanisms. *Bioimaging.* 3:49–63.
- Sheppard, C. J. R., and P. Torok. 1997. An electromagnetic theory of imaging in fluorescence microscopy, and imaging in polarization fluorescence microscopy. *Bioimaging.* 5:205–218.
- Squire, A., P. J. Verveer, and P. I. H. Bastiaens. 2000. Multiple-frequency fluorescence lifetime imaging microscopy. *J. Microsc.* 197:136–149.
- Subramaniam, V., Q. S. Hanley, A. H. A. Clayton, and T. M. Jovin. 2002. Photophysics of green and red fluorescent proteins: some implications for quantitative microscopy. *Methods Enzymol.* In press.
- Szmazinski, H., R. Jayaweera, H. Cherek, and J. R. Lakowicz. 1987. Demonstration of an associated anisotropy decay by frequency-domain fluorimetry. *Biophys. Chem.* 27:233–241.
- Thevenin, B. J. M., N. Periasamy, S. B. Shohet, and A. S. Verkman. 1994. Segmental dynamics of the cytoplasmic domain of erythrocyte band 3 determined by time-resolved fluorescence anisotropy: sensitivity to pH and ligand binding. *Proc. Natl. Acad. Sci. U.S.A.* 91:1741–1745.
- Tramier, M., K. Kemnitz, C. Durieux, J. Coppey, P. Denjean, R. B. Pansu, and M. Coppey-Moisan. 2000. Restrained torsional dynamics of nuclear DNA in living proliferative mammalian cells. *Biophys. J.* 78: 2614–2627.
- Varma, R., and S. Mayor. 1998. GPI-anchored proteins are organized in submicron domains at the cell surface. *Nature.* 394:798–801.
- Vergani, B., M. Kintrup, W. Hillen, H. Lami, E. Piemont, E. Bombarda, P. Alberti, S. M. Doglia, and M. Chabbert. 2000. Backbone dynamics of Tet repressor  $\alpha 8\text{na}9$  loop. *Biochemistry.* 39:2759–2768.
- Verkman, A. S., M. Armijo, and K. Fushimi. 1990. Construction and evaluation of a frequency-domain epifluorescence microscope for lifetime and anisotropy decay measurements in subcellular domains. *Biophys. Chem.* 40:117–125.
- Verveer, P. J., A. Squire, and P. I. H. Bastiaens. 2000. Global analysis of fluorescence lifetime imaging microscopy data. *Biophys. J.* 78: 2127–2137.
- Volkmer, A., V. Subramaniam, D. J. S. Birch, and T. M. Jovin. 2000. One- and two-photon excited fluorescence lifetimes and anisotropy decays of green fluorescent proteins. *Biophys. J.* 78:1589–1598.
- Wang, X. F., T. Uchida, D. M. Coleman, and S. Minami. 1991. Fluorescence pattern analysis based on the time-resolved method. *Appl. Spectrosc.* 45:360–366.
- Weast, R. C. 1979. *Handbook of Chemistry and Physics*. CRC Press, Inc., Boca Raton, Florida.
- Weber, G. 1977. Theory of differential phase fluorometry: detection of anisotropic molecular rotations. *J. Chem. Phys.* 66:4081–4091.
- Weber, G. 1978. Limited rotational motion: recognition by differential phase fluorometry. *Acta A. Phys. Polon.* A54:859–865.
- Wieb van der Meer, B. 1993. Fluidity, dynamics and order. In *Biomembranes: Physical Aspects*. Meir Shinitzky, editor. VCH Publishers, Weinheim, Germany. 97–158.